CLIMATE SIMULATIONS WITH GFDL SPECTRAL MODELS OF THE ATMOSPHERE: EFFECT OF SPECTRAL TRUNCATION

S. Manabe, D. G. Hahn, and J. L. Holloway, Jr.

Geophysical Fluid Dynamics Laboratory/NOAA
Princeton University
Princeton, New Jersey, USA

ABSTRACT

The climate simulation performance of three semi-spectral models differing only in spectral resolution is evaluated and compared. As the spectral resolution is increased, tropical rainbelts become narrower and better defined, subtropical dry zones expand, and the sea level pressure gradient between the subtropics and subpolar regions increases. While these spectral models maintain a level of eddy kinetic energy which is less than observed, they tend to underestimate the transient component of eddy kinetic energy and overestimate the stationary component. In general, the spectral climate models are able to simulate many of the large scale features of climate, and the quality of the simulations tends to improve with increasing spectral resolution.

Comparison is made between the performance of these semi-spectral climate models and that of finite difference climate models which have been developed at the Geophysical Fluid Dynamics Laboratory. With some exceptions, the simulated climates of the spectral models compare favorably with those of the finite difference models of comparable resolution.

1. Introduction

One of the main objectives of this study is to evaluate the capability of spectral general circulation models in simulating the earth's climate.

It has been suggested that the spectral technique of evaluating the dynamical equations is an attractive alternative to the finite difference technique because of its ability to compute spatial derivatives accurately. However, the full spectral technique has seldom been incorporated into high resolution climate models because the amount of computer time required for numerical time integration of a spectral model increases rapidly with increasing spectral resolution.

Fortunately, it has become possible to reduce the required amount of computer time by using the "transform method" proposed by Orsag (1970) and Eliassen *et al.* (1970). Adopting this technique, Bourke (1974), Hoskins and Simmons (1975), and Gordon (1979) developed "semi-spectral" baroclinic models of the atmosphere. At the Geophysical Fluid Dynamics Laboratory of NOAA, Gordon is currently conducting an extensive test of his spectral model's capability of forecasting weather. Encouraged by the positive results of his testing, a climate model is developed by the Climate Dynamics Group of GFDL, by combining Gordon's spectral dynamics with a previously developed component of the climate model in which various physical processes are incorporated.*

The climate of the earth is simulated by spectral models with three different spectral truncations. By comparing the performance of these spectral models with one another, the effect of spectral resolution upon climate simulation is evaluated. In addition, climates simulated by the spectral models are compared with the climates obtained from the finite difference general circulation models which have also been developed at GFDL. Since the parameterizations of the physical processes

---

*Recently, a spectral climate model has also been developed by Bourke *et al.* (1977). Refer to the paper by McAvaney, Bourke and Puri in this volume for additional description of the climate simulated with their model.

contained in the grid and spectral models are nearly identical, the intercomparisons essentially constitute the evaluation of the spectral methods versus the GFDL-version of the finite difference representations of the dynamical processes.

The scope of this study is not exhaustive as the intercomparisons involve the evaluation of the fields of only a few key climatic variables. However, it is hoped that this study will be useful in the planning and design phase of future numerical simulation experiments using global general circulation models.

For further comparison of the results with those of other modeling groups, additional maps and cross sections of various fields are presented without discussion in the Appendix of this paper.

2. Brief Description of the Models

Spectral models differ from gridpoint models in that the dynamic variables are represented by the synthesis of a finite sum of Legendre spherical harmonics rather than by values on a network of discrete points. The model's equations predict spectral components rather than variables at gridpoints.

In the models described here, the aforementioned transform method is used. In this method the appropriate spectral fields are transformed to a spatial grid of required resolution. Nonlinear terms are evaluated on this grid and the results of these computations are inverse transformed back into the spectral domain.

The prognostic variables of the spectral models are relative vorticity, divergence, temperature, mixing ratio and the logarithm of surface pressure. These variables are all scalars since spectral representation of vector quantities introduces singularities at the poles. When wind components are represented spectrally they are multiplied by the cosine of latitude to eliminate polar singularities.

The models adopt the hydrostatic approximation and use sigma coordinates in the vertical dimension to incorporate the effects of spatially-varying topography. A simple horizontal viscosity is incorporated into the model by reducing the tendency of model variables by a constant

times ∇^4 of the variable. In the vertical a simple mixing length diffusion scheme is used in the models.

The horizontal resolution of these models is determined by the degree of truncation of the spectral components. Three truncation limits have been used, namely, 15, 21 and 30 waves, and these limits apply in both the longitudinal and meridional directions. The so-called rhomboidal truncation has been adopted for these models. The resolution of the transform grid is a function of the truncation limit M. The number of latitudes must be at least (5M + 1)/2 and the number of gridpoints on a latitude circle, at least 3M + 1. The grid points are placed at the so-called Gaussian latitudes which are nearly equally spaced in the meridional direction. The resolution of the latitude-longitude grid corresponding to the three truncation limits is given in Table 1. Surface elevation is prescribed at the gridpoints using a method described in the Appendix.

Table 1. Parameters of the latitude-longitude grid for the M15, M21 and M30 spectral models.

Model	Latitudes	Longitudes	East-West Grid Spacing
M15	40	48	7.5°
M21	54	64	5.625°
M30	80	96	3.75°

The models have nine unevenly spaced sigma levels in the vertical (σ = (pressure/surface pressure) = 0.025, 0.095, 0.205, 0.350, 0.515, 0.680, 0.830, 0.940, 0.990). The vertical spacing is chosen so as to allow resolution of the lower stratosphere and the Ekman boundary layer.

The computed model variable tendencies are time integrated by a semi-implicit time integration scheme. Linear and nonlinear components of the tendencies are separated and time integrated implicitly and explicitly, respectively. Robert (1966) time smoothing with α = 0.01 for low resolutions is applied at each time step. For M = 30 resolution α = 0.04.

The physical processes which are incorporated into the model are nearly identical with that used in previous GFDL general circulation models (see, for example, Holloway and Manabe, 1971). A brief description of these processes follows.

The radiation scheme, which is described by Stone and Manabe (1968), is used after minor modification. For the computation of solar radiation flux, the seasonal variation of insolation is prescribed at the top of the model atmosphere. The depletion of solar radiation and the transfer of terrestrial radiation is computed taking into consideration the effects of clouds, water vapor, carbon dioxide and ozone. The mixing ratio of carbon dioxide is assumed to be constant everywhere. A zonally uniform distribution of ozone is specified as a function of latitude, height, and season. For simplicity, cloud cover is assumed to be zonally uniform and invariant with respect to time. The distribution of water vapor is determined from the time integration of the prognostic equation of water vapor which involves the three-dimensional advection of water vapor, vertical mixing of water vapor in the planetary boundary layer, evaporation, nonconvective condensation, and moist convective adjustment proposed by Manabe *et al.* (1965).

Surface temperatures over continents are determined by the boundary condition that no heat is stored in the soil, i.e., net fluxes of solar and terrestrial radiation and turbulent fluxes of sensible and latent heat locally add to zero. Over the oceanic part of the models, the seasonal variation of surface temperature is prescribed. It is determined by interpolating in time between four observed distributions of monthly mean sea surface temperatures obtained from the U.S. Naval Oceanographic Office (1944, 1957, 1958, 1967a,b, 1969). For the computation of the net downward flux of solar radiation, the surface albedos are prescribed as a function of latitude over oceans and pointwise over land. These albedos, however, are replaced by higher values whenever snow cover or sea ice are simulated.

The schemes for computing the hydrology of the earth's surface are similar to those described by Manabe (1969). The rates of change of soil moisture and snow depth are determined by the budget of water, snow and heat at the ground surface.

Results from the spectral models are compared with those of grid point models on modified global Kurihara-Holloway type grids (Kurihara and Holloway, 1967) having mean horizontal resolutions of 500 km and 250 km. Descriptions of the grid point models are found in Holloway and Manabe (1971), Manabe and Holloway (1975), Manabe *et al.* (1970a), Manabe *et al.* (1974), Manabe and Mahlman (1976) and Manabe and Terpstra (1974).

3. Experimental Design

All three spectral models are time-integrated with prescribed seasonally varying insolation and sea surface temperatures, similar to the time-integration of the grid point models as described by Manabe *et al.* (1974). The periods of time-integration for the M15, M21, and M30 spectral models are shown in Fig. 1. Initial conditions for the M15 and M21 models are taken from the last day of a long term perpetual January M15 simulation experiment. The M15 experiment is then time-integrated for approximately 2.5 model years and terminates on model date 1 August. The M21 experiment is time-integrated for more than 3 model years and terminates on model date 1 July. The results from the last year of these seasonal time-integrations are presented in this paper.

The M30 spectral model has not been time-integrated for a complete model year because of the large computer time requirements (see Section 6). Instead, two separate time-integrations are performed for the simulation of the summer and winter seasons. Initial conditions for the January M30 simulation are taken from 7 December M15 spectral model results. Initial conditions for the July simulation are taken from the 31 May M21 spectral model results.

As previously noted, the grid model results used for comparison are taken from previously published sources. Results depicting a 500 km grid model performance are taken from the last 70 days of a 341 day perpetual January time integration (Holloway and Manabe, 1971). Results depicting a 250 km grid model performance are taken from two sources, namely, the last 36 days of a 70-day perpetual January time integration (Holloway and Manabe, 1971), and the last year of a 2.5 year annual

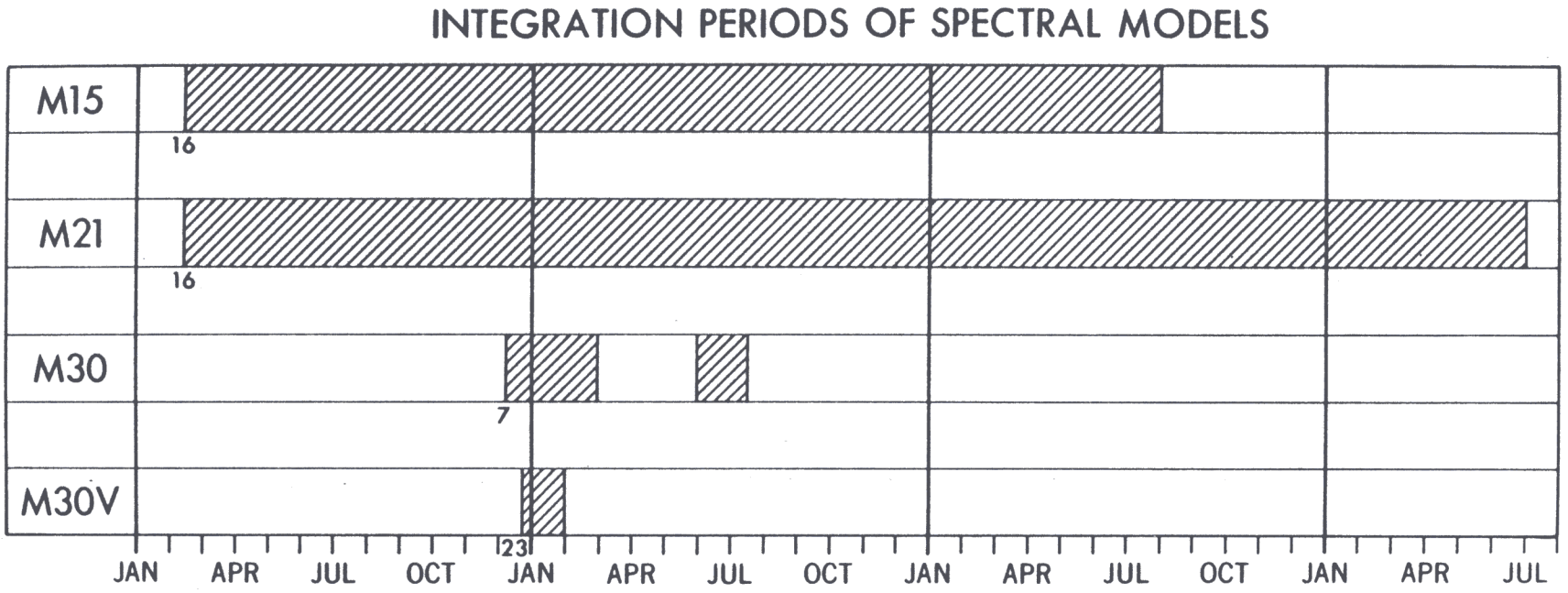

Fig. 1. Bar graphs indicating the period of time-integration of the M15, M21, M30 and M30V spectral models.

experiment (Manabe *et al.*, 1974; Manabe and Holloway, 1975; Manabe and Mahlman, 1976). By comparing results from these two grid resolutions with those of the three spectral resolutions, it is hoped that one will be better able to understand not only the effects of model resolution but also the relative performance of spectral vs. grid representations of the dynamical processes in these GFDL general circulation models.

In the previous section, it was stated that the spectral models have a horizontal viscosity formulation of the form $a \nabla^4 b$, where a is a constant and b is any model prognostic variable. All three spectral simulation experiments use the same value of the viscosity coefficient, namely, $10^{24} cm^4/sec$. For the evaluation of the effect of changing the value of the coefficient of viscosity, a second spectral January simulation experiment (M30V) is time-integrated in which the value of a is reduced to one-quarter that in the previous M30 experiment. Initial conditions for this experiment are taken from model date 23 December of the M30 experiment, and the M30V model is time-integrated through model date 1 February. Results from this experiment are briefly compared with those of the M30 spectral results to illustrate the effects of changing the value of the coefficient of viscosity a in the spectral models.

4. Spectral Model Intercomparisons

4.1. *Sea level pressure*

Figure 2 contains geographical distributions of January mean sea level pressure from the M15, M21 and M30 spectral models. For comparison, the observed January sea level pressure distribution (Crutcher and Meserve, 1970, and Taljaard *et al.*, 1969) is also shown in Fig. 2. For the low resolution M15 model, the fidelity of the January mean sea level pressure simulation is better than expected. For example, the subtropical highs west of Africa and North and South America and the continental lows over Africa and South America are well simulated. Furthermore, the latitudinal positions of the subtropical high pressure belts (near 30N and 30S), are very well located in the M15 spectral model. This is evident in Fig. 3, which illustrates latitudinal distributions of simulated and observed zonal mean sea level pressure. As Fig. 3 indicates,

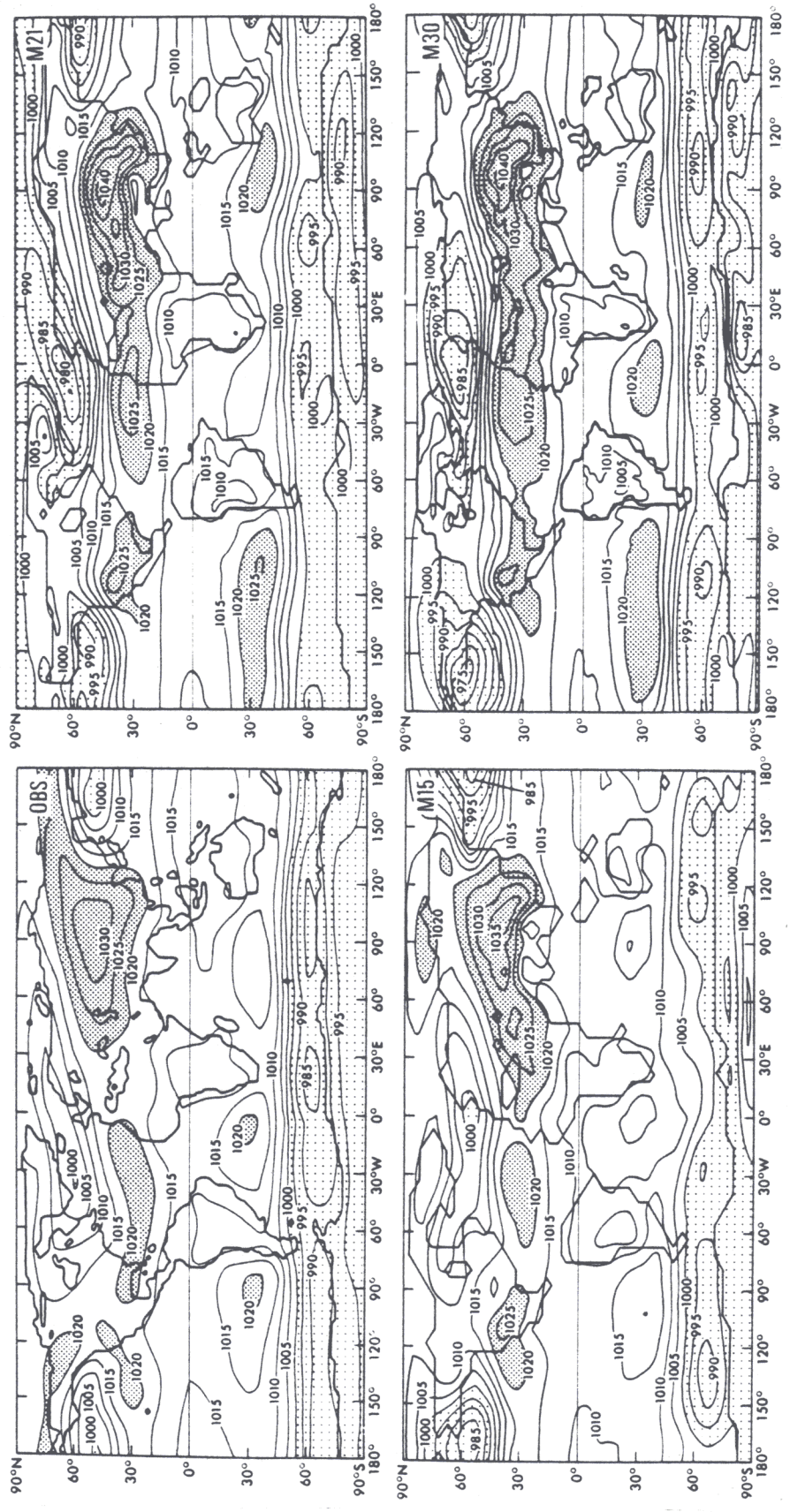

Fig. 2. Geographical distributions of the January mean sea level pressure (mb) for the M15, M21 and M30 spectral models and observed (Crutcher and Meserve, 1970, and Taljaard *et al.*, 1969).

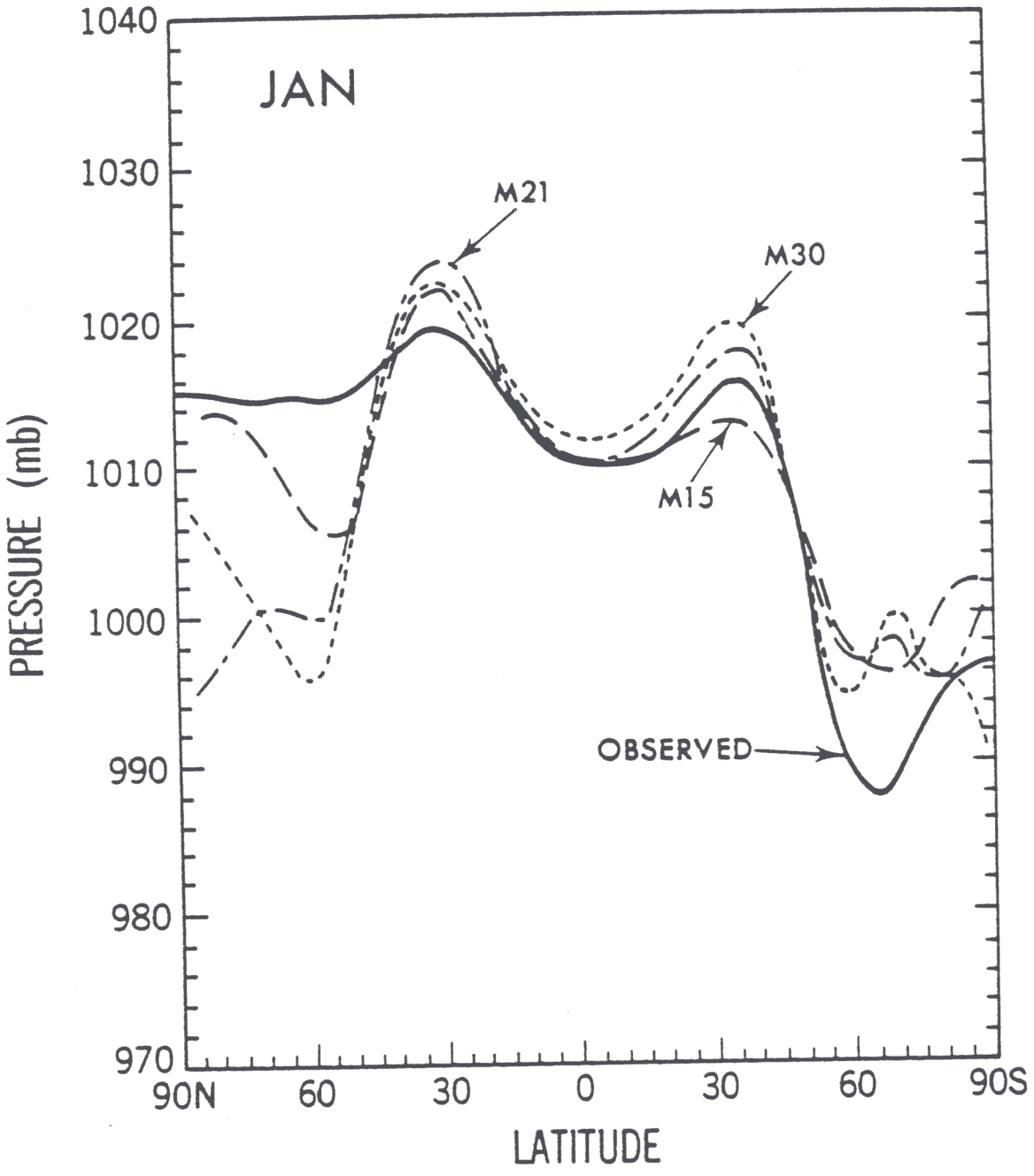

Fig. 3. Latitudinal distributions of the January zonal mean sea level pressure (mb) for the M15, M21 and M30 spectral models and as observed (Crutcher and Meserve, 1970, and Taljaard *et al.*, 1969).

the M15 spectral model maintains subpolar low pressure belts near 60N and 60S. While the latitudinal positions of the subpolar low pressure belts are realistic, the intensity of the northern belt is too strong while that of the southern belt is too weak. In the Northern Hemisphere, this shortcoming is mainly a manifestation of the Aleutian low being too deep. In addition, the Siberian High is too intense and the combination of these deficiencies results in the low-level northwesterly flow near Japan being much too strong in the M15 spectral model results.

As the spectral resolution is increased from M15 to M21 and M30, there is a tendency for some of the large-scale pressure features to become more intense, i.e., higher resolution spectral models tend to have a deeper low pressure belt near 60N and belts of higher pressure near 30N and 30S. As a result, the higher resolution spectral models tend to have steeper gradients between 30 and 60 degrees of latitude, creating stronger westerlies in both hemispheres in January. This increase in the midlatitude north-south pressure gradient with increasing spectral resolution further aggravates the tendency for too strong westerly flow as shown in the results of the M15 spectral model for the Northern Hemisphere in January. However, this increase substantially improves the spectral simulation of the belt of strong westerly flow in the midlatitudes of the Southern Hemisphere. As pointed out in Section 5, comparable fidelity in simulating the flow patterns north of the Antarctic coast is not achieved by a high resolution global GFDL grid model having similar physics.

For the simulation of sea level pressure, the general performance of the spectral models is somewhat better for July than for January. This is evident in Figs. 4 and 5 which show the geographical and zonal mean distributions of July mean sea level pressure for the three spectral models (M15, M21, M30) along with the observed distribution (Crutcher and Meserve, 1970, and Taljaard *et al.*, 1969). For July, all spectral models simulate the zonal mean sea level pressure profile reasonably well. Increasing the spectral resolution results mainly in enhancing the pressure gradient between 30S and 65S.

Examining the geographical distributions of July mean sea level pressure which are shown in Fig. 4, one notes that subtropical highs are usually more intense in higher resolution models. This tendency

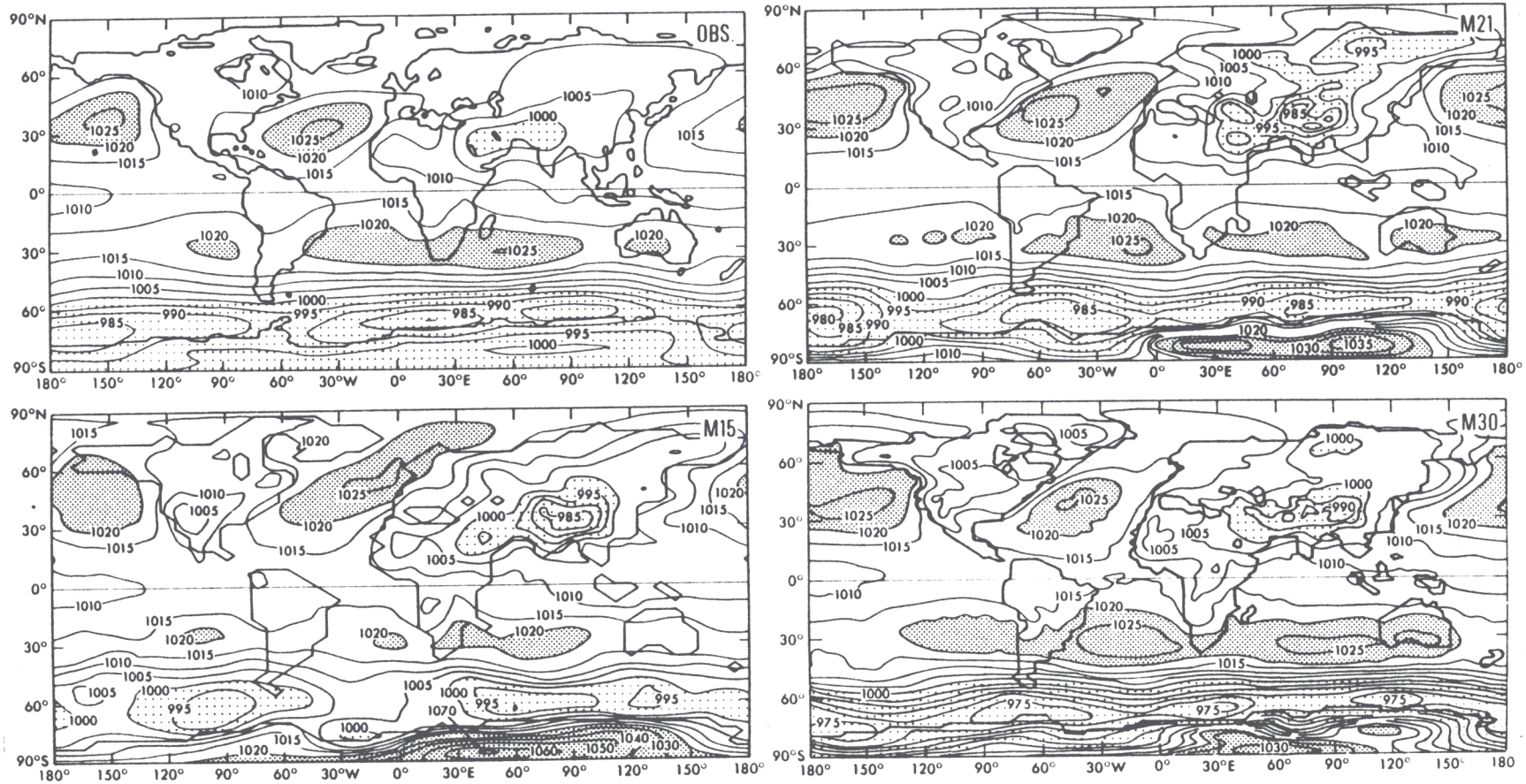

Fig. 4. Geographical distributions of the July mean sea level pressure (mb) for the M15, M21 and M30 spectral models and observed (Crutcher and Meserve, 1970, and Taljaard *et al.*, 1969).

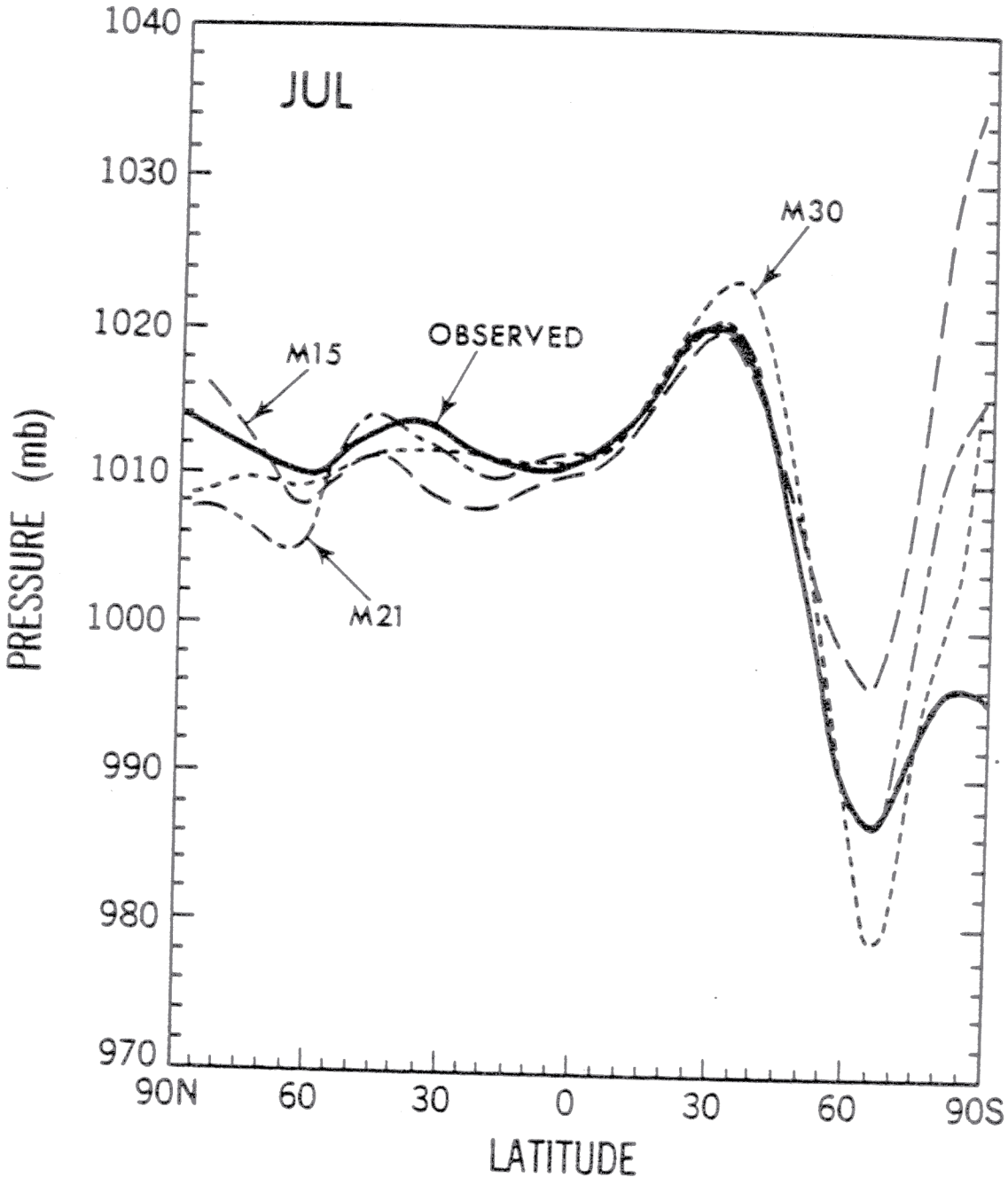

Fig. 5. Latitudinal distributions of the July zonal mean sea level pressure (mb) for the M15, M21 and M30 spectral models and as observed (Crutcher and Meserve, 1970, and Taljaard *et al.*, 1969).

is particularly evident in the Southern Hemisphere. Figure 4 also indicates that the location and the shape of subtropical highs over the North Pacific and the North Atlantic are more realistic in the M30 than in the M15 simulation. It is of interest that the intensity of not only the subtropical highs around 30S but also of the low pressure belt around 60S increase with increasing spectral resolution, resulting in successful simulation of the midlatitude belt of strong westerlies in the Southern Hemisphere by both the M21 and the M30 models. This is particularly encouraging since all previous GFDL models have failed to reproduce this feature as discussed in Section 5. Figure 6, which shows a daily map of surface stream lines from the M30 model, clearly indicates that this model successfully reproduces a train of cyclones which is observed along the periphery of the Antarctic Continent.

It is disturbing that the simulation of sea level pressure over the Antarctic Continent is very poor. Because of the altitude of the continent, the value of sea level pressure depends very much upon the assumptions used for sea level reduction. This is a subject of future investigation.

Figure 4 indicates that the spectral models tend to exaggerate the intensity of continental lows over South Asia and the southern part of North America. This tendency is particularly evident in the high resolution simulations. It results in the overprediction of land-sea contrast in sea level pressure and produces excessive southerly flow along the east coast and excessive northerly flow along the west coast of these continents. The cause of this difficulty has not yet been identified.

In summary, it is clear that, despite some exceptions identified in the preceding paragraph, the simulation of July mean sea level pressure generally improves with increasing spectral resolution.

4.2. *Upper tropospheric flow*

A streamline map of the January mean 205 mb flow field for all three spectral models is shown in Fig. 7a. A similar set of maps is shown in Fig. 7b for the July mean upper tropospheric flow. Observed January and July 200 mb flow patterns (Sadler, 1975) are shown in Fig. 8. In both

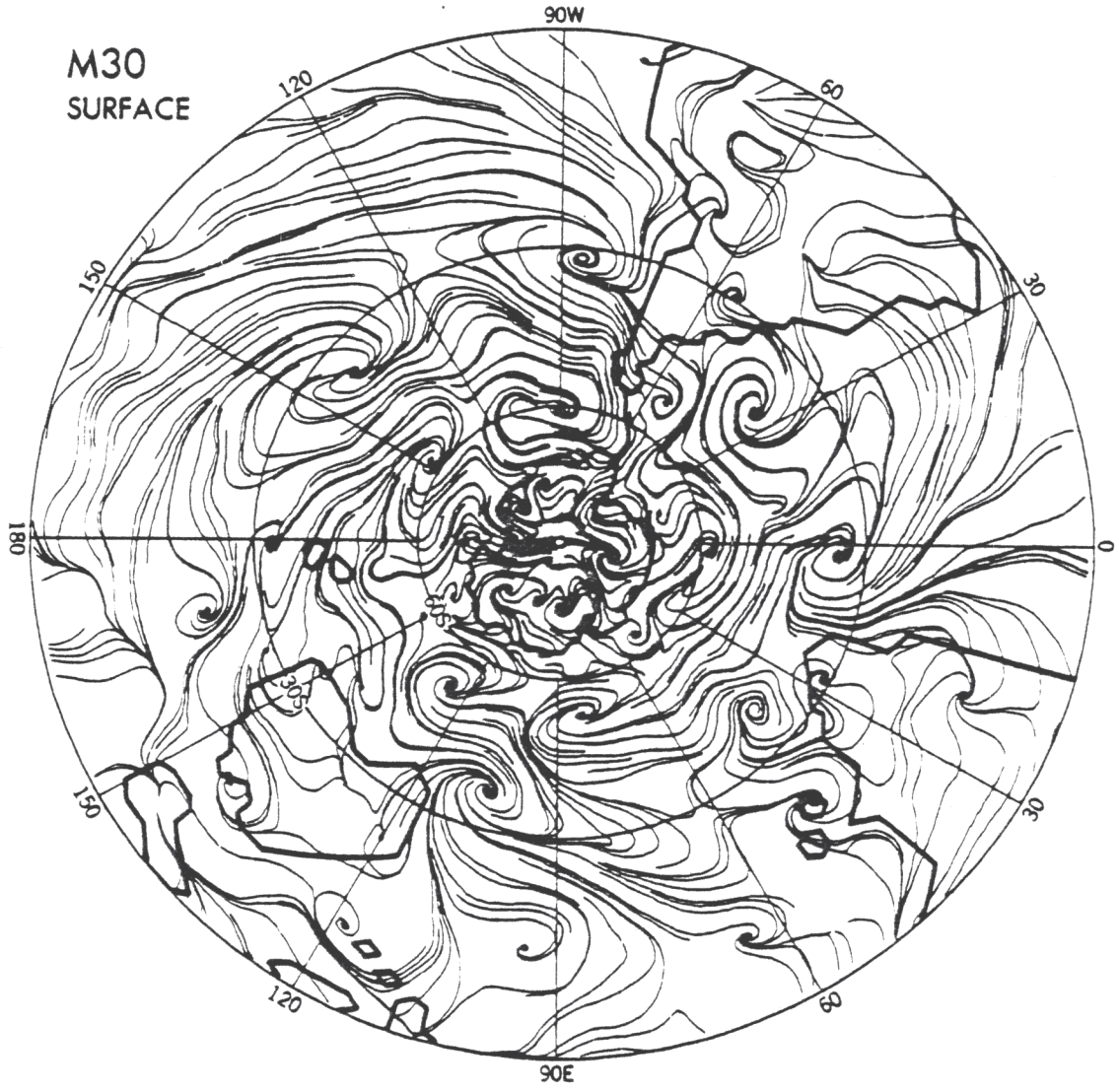

Fig. 6. Stereographic Southern Hemisphere surface streamline map of 15 January of the M30 model simulation.

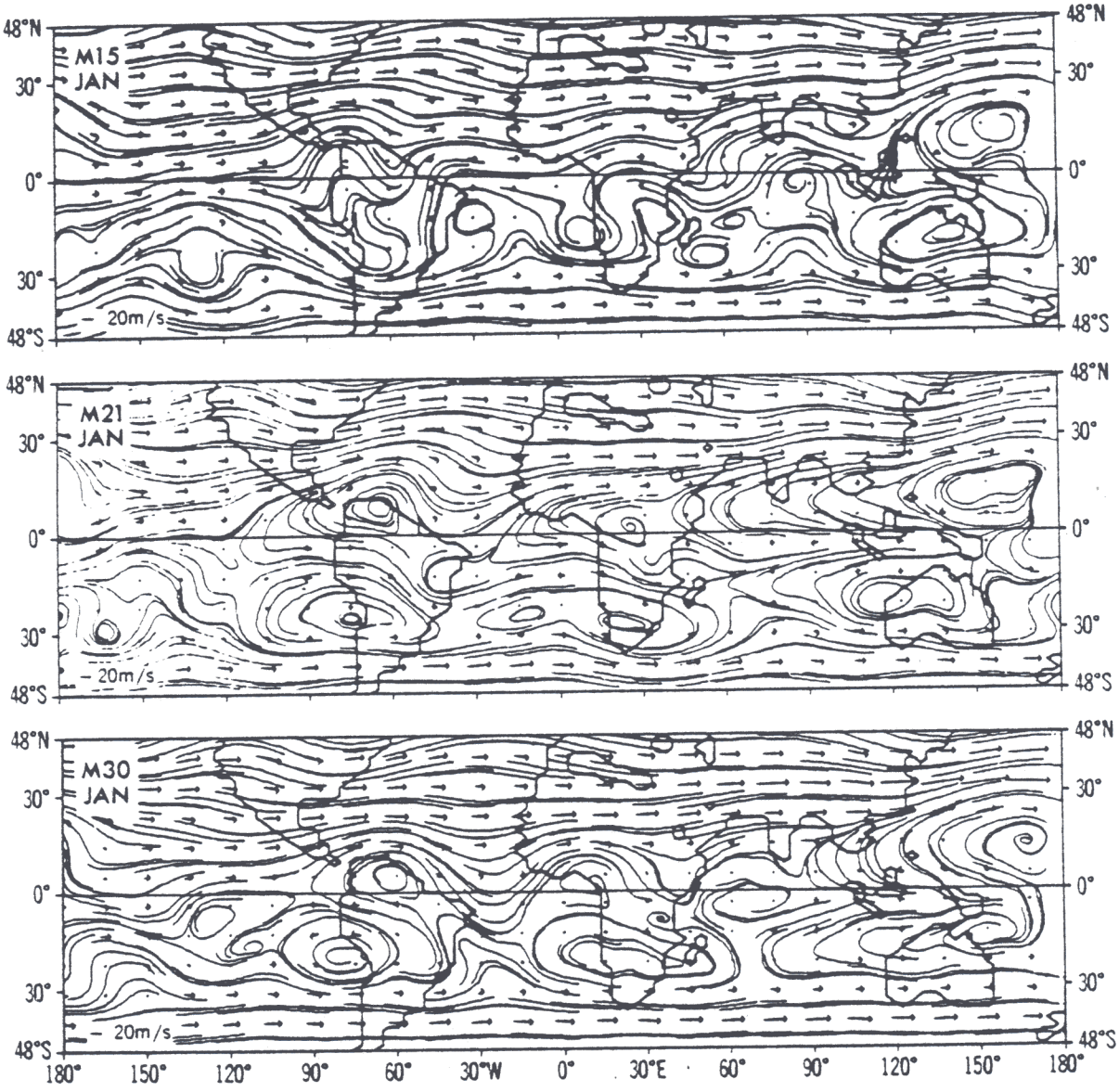

Fig. 7a. January mean vectors and streamlines at the 205 mb level of the M15, M21 and M30 spectral models.

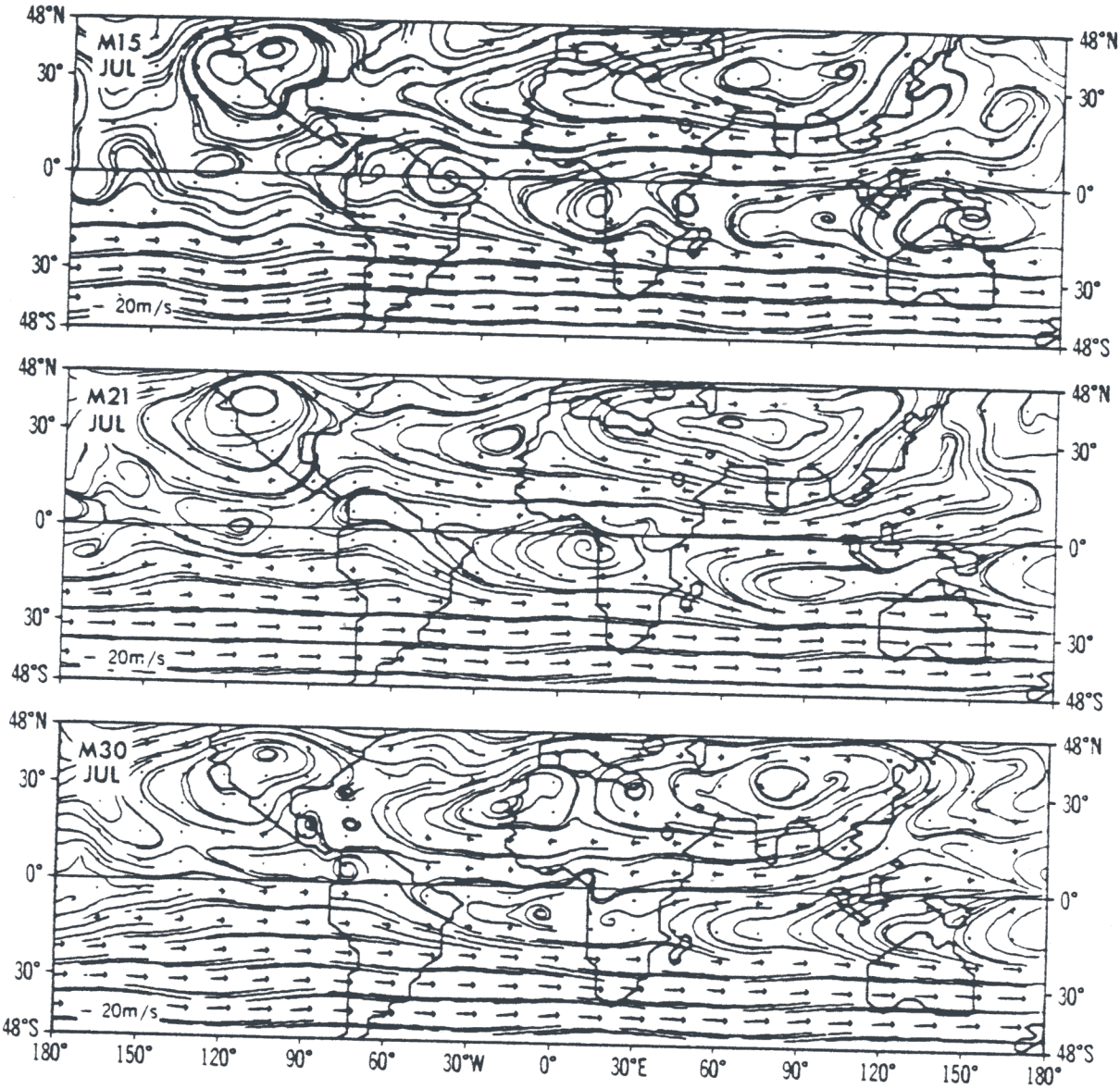

Fig. 7b. July mean vectors and streamlines at the 205 mb level of the M15, M21 and M30 spectral models.

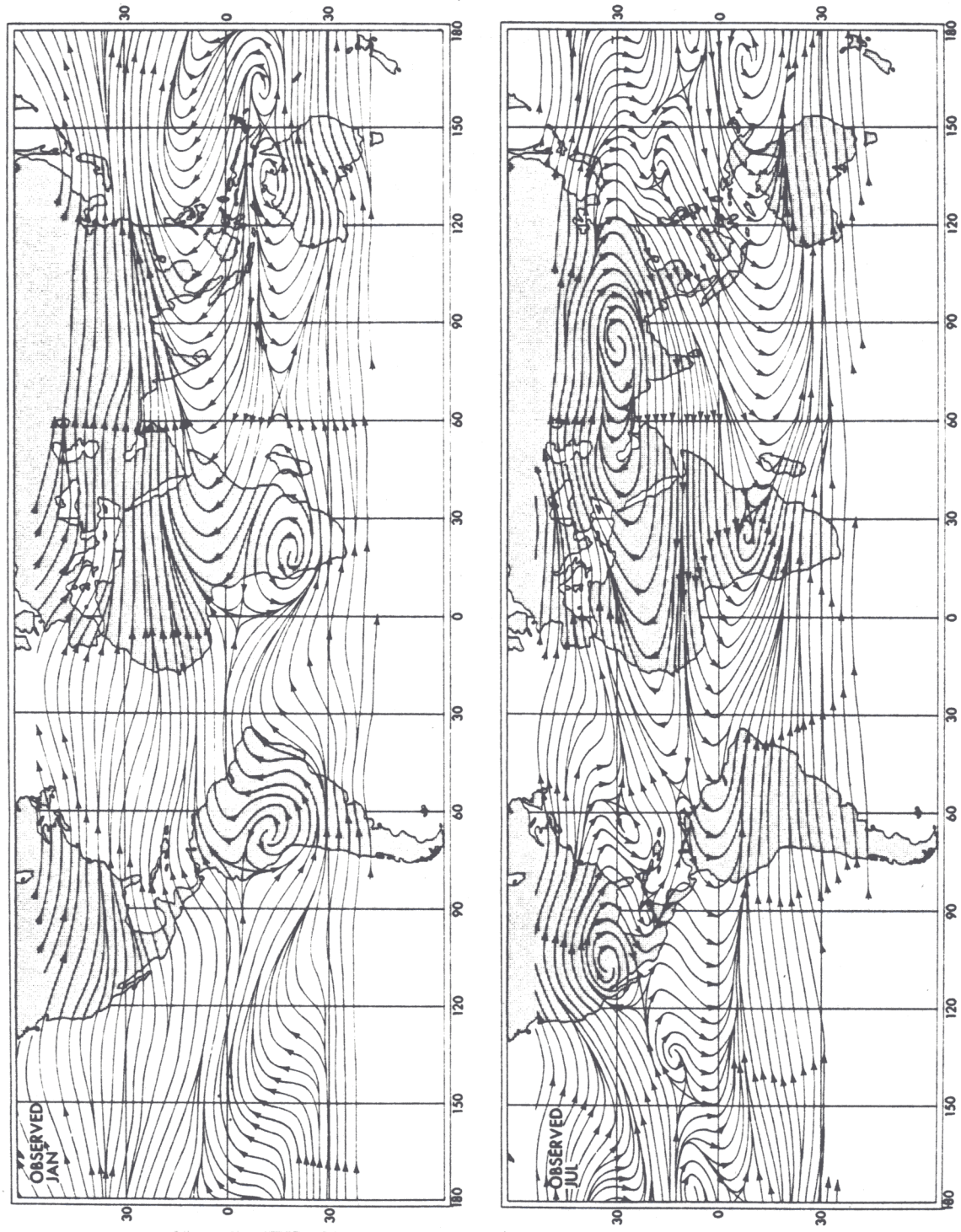

Fig. 8. Observed mean January and July streamline distributions at the 200 mb level (Sadler, 1975).

months, much of the interhemispheric exchange near the 200 mb level is associated with anticyclonic circulation pairs which straddle the equator. In January, southeasterly flow crosses the equator over Africa, the western Pacific and South America; in July the flow is reversed. In the low resolution (M15) model, anticyclonic circulation pairs tend to be abnormally weak in January resulting in limited interhemispheric exchange. However, the models with increased spectral resolution tend to have anticyclonic pairs which are more intense and well-defined giving rise to increased cross-equatorial flow. In July over the equatorial region of the Indian Ocean, the meridional component of the upper tropospheric monsoon return flow is greater in the M30 experiment than in the M15 and M21 experiments.

Additional structure in the upper tropospheric flow is associated with the mid-oceanic troughs which predominate in the summer season over the North and South Pacific and the North and South Atlantic. Those troughs in the Southern Hemisphere actually extend across the equator and account for cross-equatorial flow during January (see observed distribution in Fig. 8). In the January simulations of the upper tropospheric flow, the M15 model produces rather weak troughs in the equatorial regions of the South Pacific and South Atlantic. In the higher resolution models, these features tend to be sharper and more intense. In the South Atlantic, the mid-oceanic trough in the M30 simulation lies along the eastern coast of South America, in close agreement with the observed distribution. However, in the South Pacific, the mid-oceanic trough is shifted approximately 30 degrees west of its observed position in the M30 model results. This westward shift is probably related to the presence of a trough, not present in the observed analysis, which persists in the equatorial regions of the mid-North Pacific and extends across the equator into the Southern Hemisphere.

In July the mid-oceanic trough over the North Atlantic is simulated by all three spectral models. Over the North Pacific, the trough is oriented more north-south in the M15 model, a pattern which tends to agree with the mean observed June-July-August flow in 1967 (Krishnamurti *et al.*, 1973) rather than with Sadler's climatology shown here. However, as the spectral resolution is increased from M15 to M21 and M30, the flow

patterns become progressively more like those of Sadler's climatology with the mid-Pacific trough becoming oriented more east-west and the subequatorial ridge, which parallels it to the south, becoming more well defined.

In July the flow patterns associated with the Asian high are very well simulated by all three spectral models. The anticyclonic circulation is oriented somewhat northeast-southwest in the M15 model, better resembling the flow pattern observed in August of 1972 (Krishnamurti *et al.*, 1975) than that of Sadler's climatology. Again the M21 and M30 simulations are more similar to Sadler's climatology with the axis of the Asian anticyclone being oriented more east-west and the flow to the north of the anticyclonic circulation being more westerly rather than southwesterly.

4.3. *Eddy kinetic energy*

Hemispheric integrals of eddy kinetic energy in both January and July are contained in Table 2 for all spectral models together with the observed counterpart. This table indicates that all of the spectral models maintain a relatively high level of tropospheric eddy kinetic energy. In fact, in July the M15 model maintains a level of eddy kinetic energy in the Northern Hemisphere which is nearly equal to the observed. This is encouraging since eddy kinetic energy in most general circulation models tends to be too small. In addition, the M15 model maintains more eddy kinetic energy than either the M21 or the M30 model, but this does not necessarily imply that the M15 model produces a more realistic distribution of eddy kinetic energy than the other two models. For further analysis, the spectral distribution of eddy kinetic energy is computed for all three model atmospheres and is shown in Fig. 9. At high zonal wave numbers (9-15), eddy kinetic energy in the M15 model simulation is very large compared with that in the M21 and M30 simulations, indicating a tendency for eddy kinetic energy to accumulate near the zonal wave number of spectral truncation (i.e., 15). This result suggests that the high level of eddy kinetic energy, which is maintained

Table 2. January and July hemispheric integrals of eddy kinetic energy (joules/kg) from the surface to 140 mb of the M15, M21, M30 and M30V spectral models. The corresponding integrals of observed eddy kinetic energy from the surface to 150 mb are taken from Oort (1971).

	JANUARY		JULY	
	NH	SH	NH	SH
M15	91.5	58.3	53.8	81.2
M21	78.9	45.6	43.9	67.2
M30	77.3	46.2	41.8	66.0
M30V	80.1	50.8	--	--
Obs.	105.4	--	54.4	--

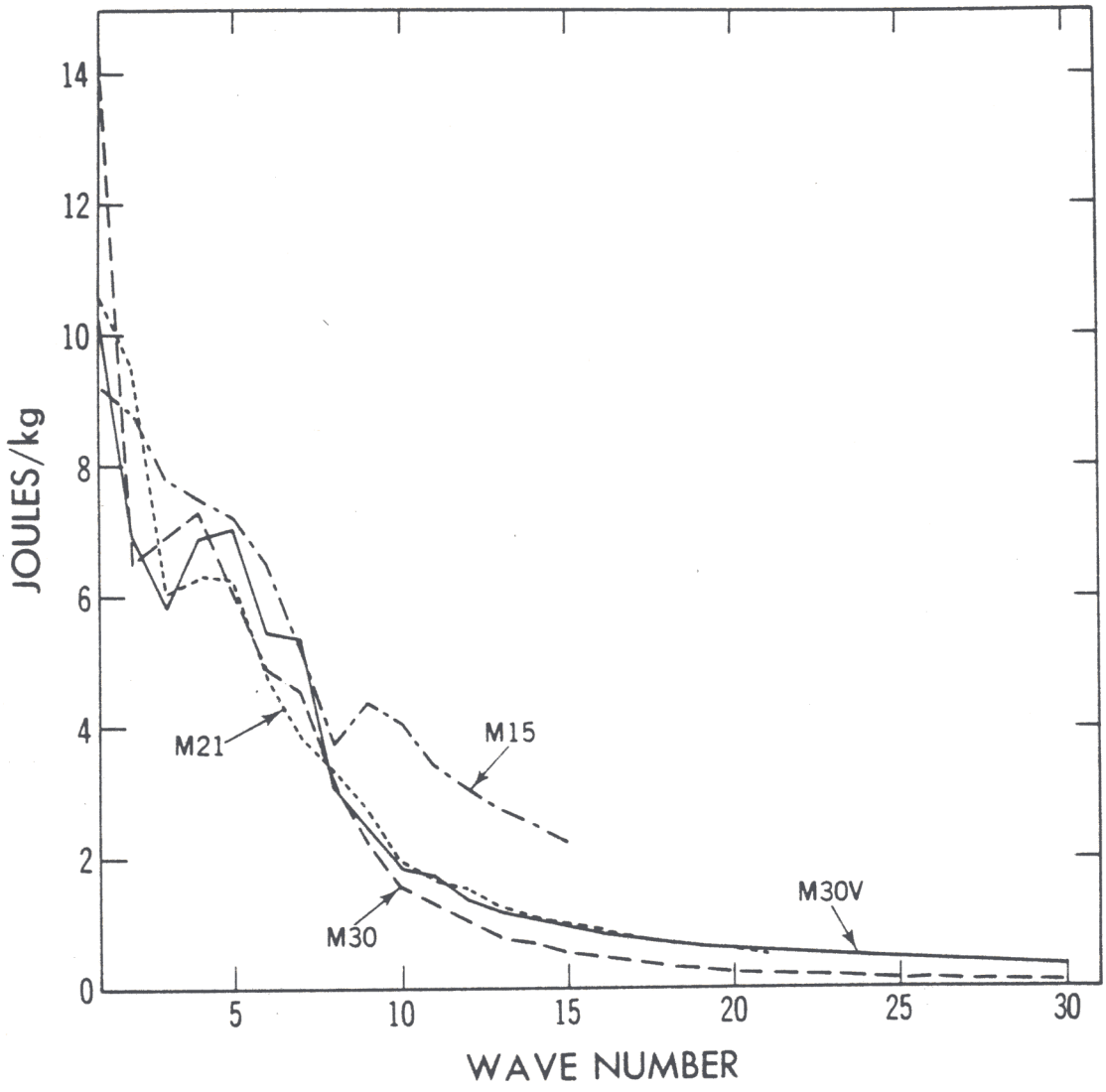

Fig. 9. Graph of January mean eddy kinetic energy (joules/kg) as a function of zonal wave number for the M15, M21, M30 and M30V models.

in the M15 model atmosphere, results in part from the pathological accumulation of energy near the wave number truncation limit. While the coefficient of the fourth order viscosity is held constant for all three experiments, the results described here appear to indicate that use of a larger coefficient would improve the performance of the M15 model.

On the other hand, the performance of the M30 model could probably be improved by reducing its viscosity coefficient. According to Fig. 10a, which shows a typical daily map of geopotential height at the 500 mb level of the M30 model in January, the flow field is too zonal to be realistic. One of the possible causes of this difficulty is the overdamping of westerly waves by excessive viscosity.

Another spectral model (M30V) is constructed and is integrated with time. This model is identical to the original M30 model except that its viscosity coefficient is smaller by a factor of 4. The impact of the viscosity reduction can be identified by a comparison of Fig. 10a with Fig. 10b which contains the corresponding 500 mb geopotential height map from the M30V experiment. In the M30V map of geopotential height, the patterns are less zonal (or westerly waves have larger amplitude) and cut-off lows, which are common to most daily 500 mb weather maps in January, become more pronounced. This result is consistent with the eddy kinetic energy statistics in Table 2 which show that the M30V model contains slightly more eddy kinetic energy than the M30 model. As Fig. 9 indicates this additional kinetic energy is distributed not only at very high zonal wave numbers, but also at zonal wave numbers 5 through 7.

In Table 3 and Table 4, the eddy kinetic energy statistics of Table 2 are further separated into stationary and transient components, respectively. While all models were previously shown to contain a 10-25 percent deficit in total eddy kinetic energy, Table 3 indicates that they maintain too much stationary eddy kinetic energy, exceeding observed values by 50-100 percent in the Northern Hemisphere. On the other hand, Table 4 indicates that transient eddy kinetic energy is too small in all

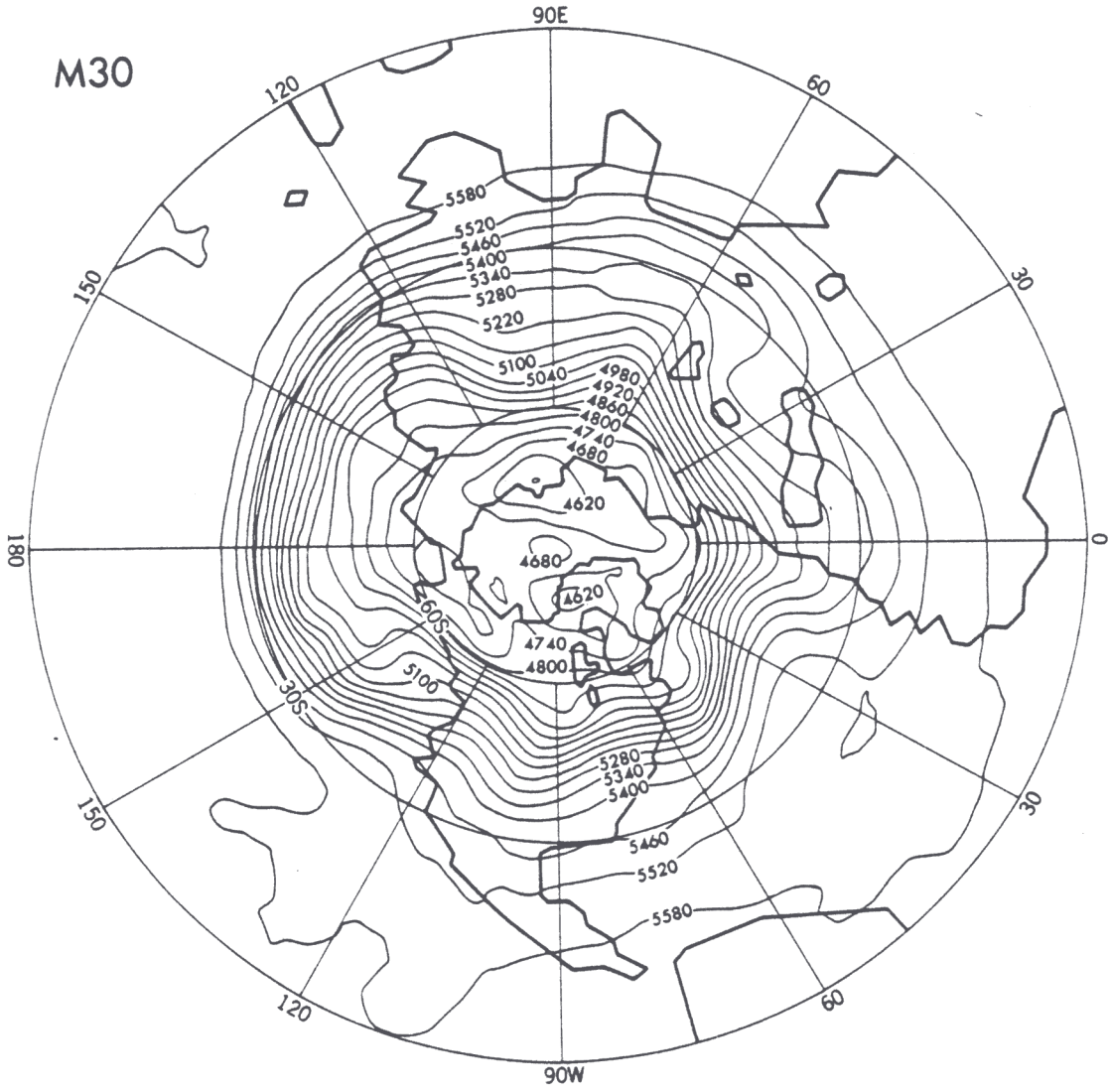

Fig. 10a. Stereographic Northern Hemisphere distribution of 500 mb geopotential height (meters) on 14 January as simulated by the M30 model.

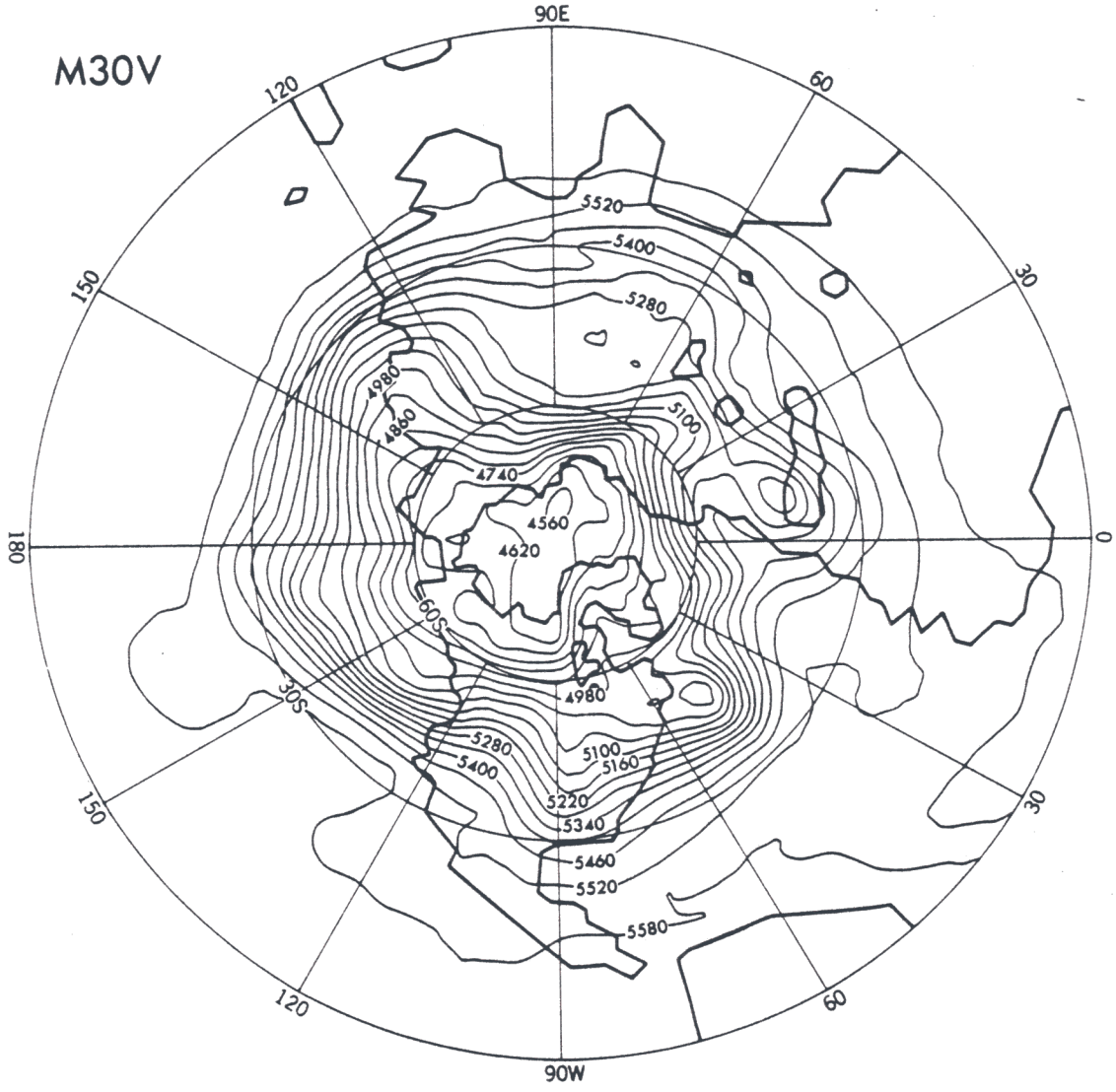

Fig. 10b. Stereographic Northern Hemisphere distribution of 500 mb geopotential height (meters) on 14 January as simulated by the M30V model.

Table 3. Same as Table 2 for the stationary component of eddy kinetic energy.

	JANUARY		JULY	
	NH	SH	NH	SH
M15	25.5	8.5	12.7	9.7
M21	31.1	10.0	13.7	7.8
M30	32.5	8.9	16.3	11.7
M30V	26.1	8.0	--	--
Obs.	16.5	--	7.8	--

Table 4. Same as Table 2 for the transient component of eddy kinetic energy.

	JANUARY		JULY	
	NH	SH	NH	SH
M15	66.0	49.8	41.1	71.5
M21	47.8	35.6	30.2	59.4
M30	44.8	37.3	25.5	54.5
M30V	54.0	42.8	--	--
Obs.	88.9	--	46.6	--

model atmospheres. In summary, all three spectral models share an inability to partition eddy kinetic energy into transient and stationary components accurately.

4.4. *Precipitation*

Geographical distributions of the January mean rate of precipitation as simulated by the three spectral models (M15, M21, M30) are shown along with the observed climatological mean in Fig. 11. The July counterparts are shown in Fig. 12. By comparing the spectral model results with the

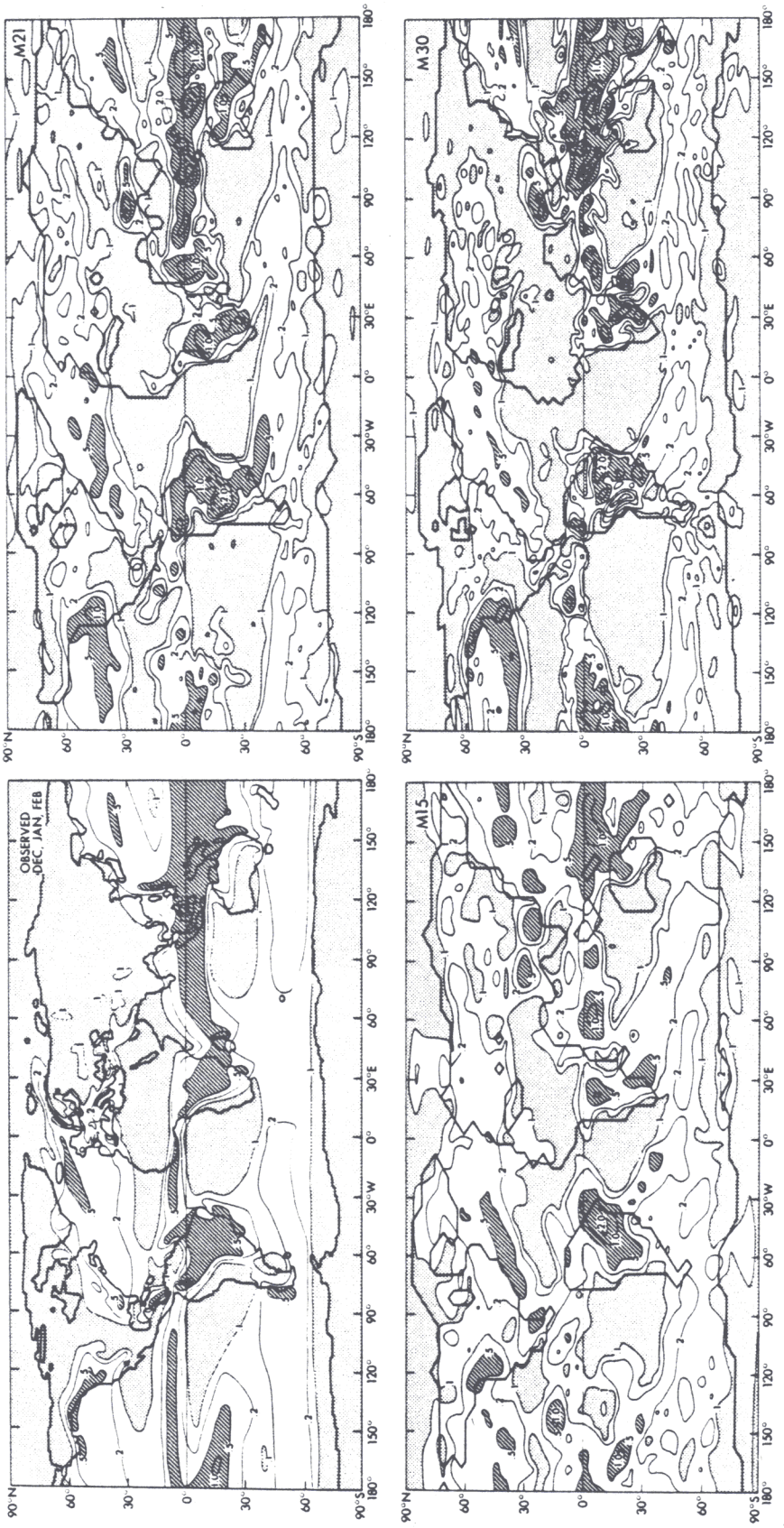

Fig. 11. Geographical distributions of the January mean rate of precipitation (cm/day) for the M15, M21 and M30 spectral models together with the observed counterpart (Möller, 1951).

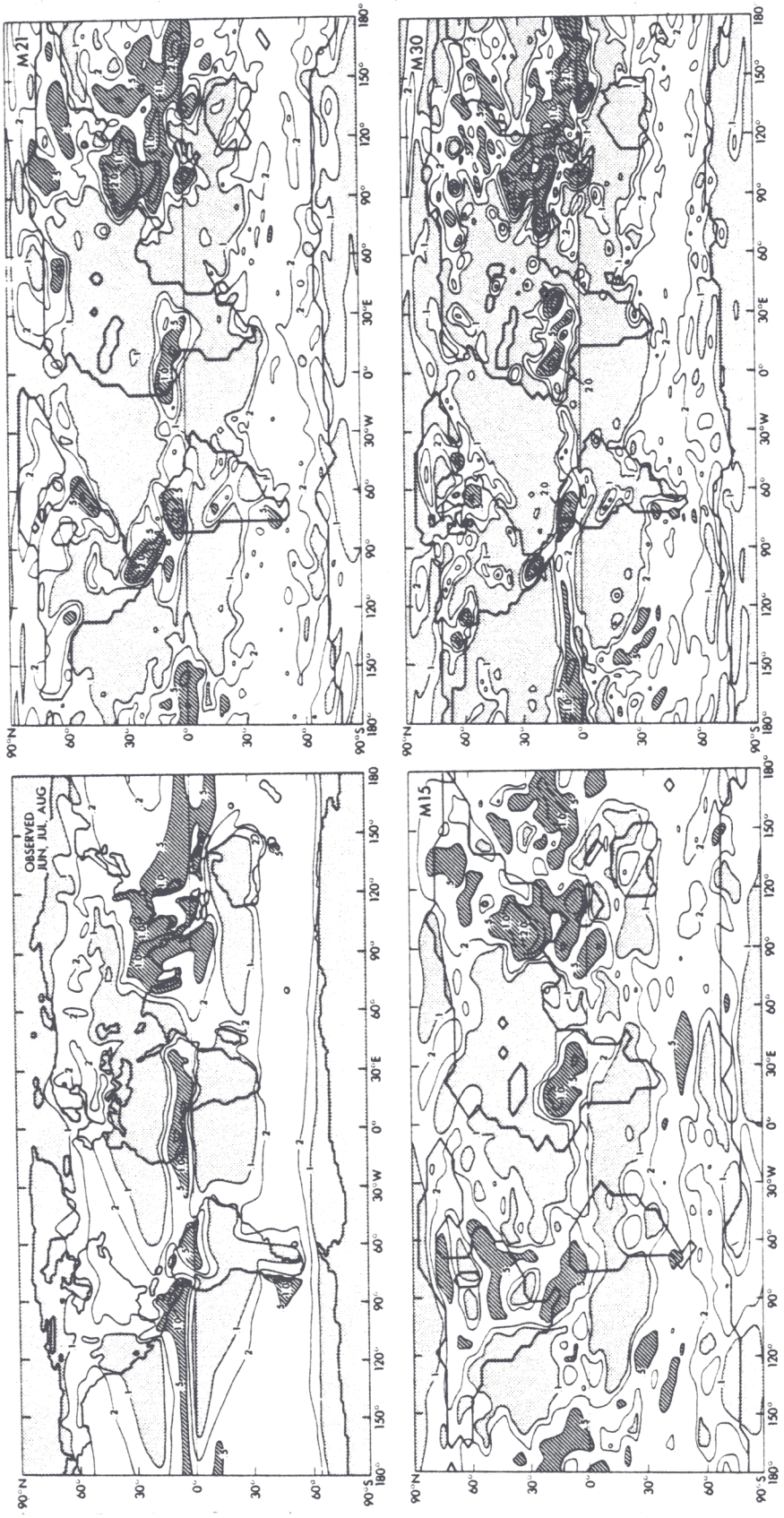

Fig. 12. Geographical distributions of the July mean rate of precipitation (cm/day) for the M15, M21 and M30 spectral models together with the observed counterpart (Möller, 1951).

climatological distributions, one can see quite clearly that the low resolution spectral model is not able to capture many of the details of the large-scale precipitation distribution in January. This is in marked contrast to the good performance of the low resolution spectral model in simulating the large-scale sea level pressure distribution. However, as the spectral resolution is increased, the fidelity of the spectral model simulation of the January precipitation distribution is greatly improved. For example, in January, increasing the spectral resolution tends to result in more well-defined rainbelts over the eastern tropical Pacific and western North America, an improved continental rainfall distribution over South America, an expanded oceanic dry zone over the Arabian Sea and expanded continental dry zones over eastern North Africa, Arabia, Asia, and central North America. Similar improvements are evident in the July distribution, and, in particular, an Asian monsoon rainfall maximum is located over central India in the high resolution M30 spectral model.

Unfortunately, there are some shortcomings in simulating the precipitation distributions which are shared by all the spectral models. For example all three models simulate too much precipitation over much of northern Asia and in a smaller region south of the Himalayas in January. The effect of increasing the spectral resolution is improvement of the problem over northern Asia; however, the results are still unsatisfactory. This problem is also evident in high resolution grid model simulations (see Section 5), and further efforts are therefore necessary to identify the cause of these common shortcomings.

In both January and July, the oceanic dry zones west of Africa and west of North and South America tend to be expanded as the spectral resolution is increased. From a comparison with the climatological mean distributions of Möller (1951), it appears that the low resolution spectral model (M15) captures the areal extent of these dry zones better than the higher resolution models. In view of the uncertainty of the rainfall measurements over oceanic areas, oceanic dry zones as reconstructed from satellite measurements of rainfall (Rao *et al.*, 1976) are presented in Fig. 13 for additional comparison. In both January and July, the above mentioned subtropical oceanic dry zones are consistently

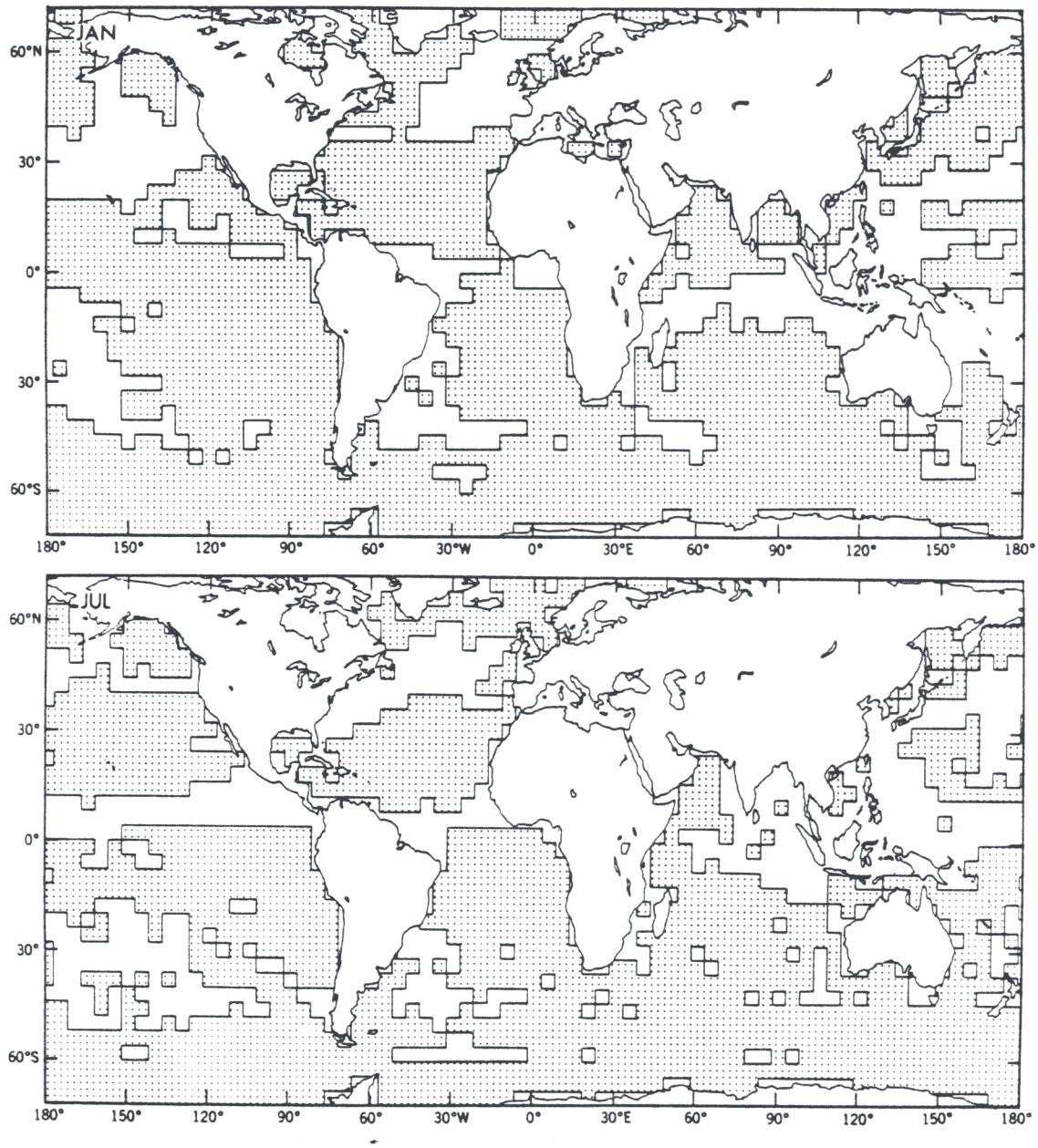

Fig. 13. Geographical distributions of oceanic dry zones as obtained from satellite derived rainfall measurements (Rao *et al.*, 1976) during January and July of 1974. Shaded areas correspond to rainfall rates of less than 0.12 cm/day.

broader in areal extent than those of the climatological distributions of Möller. Moreover, the satellite derived distributions of oceanic dry zones tend to agree very well with those of the M30 simulation.

For evaluation of the simulated climate from a somewhat different viewpoint, monthly mean fields of precipitation and surface ambient temperature are collected from model results, and from these data a climate type is derived for each region according to the classification system derived by Köppen (1931). The Köppen climate classification scheme was originally designed to delineate regions of different types of natural vegetation, such as trees, grasses, desert, etc. Therefore, this system is very useful for evaluating the capability of a model in reproducing the large-scale distribution of climatic conditions relevant for the growth of natural vegetation.

From the annual variation of precipitation and surface ambient temperature, the Köppen classification system subdivides climates of the earth into five major groups (designated "A" through "E") and a number of subtypes. Group A designates tropical rainy climates; B, desert (BW) and steppe (BS) climates; C, wet temperate regions with mild winters; D, wet temperate climates with cold winters; and E, tundra (ET) and perpetually frozen (EF) areas. A lower-case letter following the capital letter for groups A, C, and D delineates the characteristics of the seasonal variation of precipitation rate. In particular, "f" indicates areas where the precipitation is roughly evenly distributed throughout the year; "w" or "s" is used when the particular area has a dry winter or dry summer, respectively. The quantitative definition of these climate categories can be found in almost any climatology textbook. We used Haurwitz and Austin (1944) and Trewartha (1968) for adopting the most widely accepted criteria for deriving the Köppen types from the simulated model results.

Figure 14 shows the Köppen climate maps as derived from the M15 and M21 spectral data and observed data. Unfortunately, the M30 spectral Köppen map is not available since the M30 spectral model has not been time integrated for a complete model year. According to this comparison, the M21 simulation is superior to the M15 simulation of climate, reflecting mainly the difference in the capabilities of the two models in reproducing the seasonal variation of precipitation. For example,

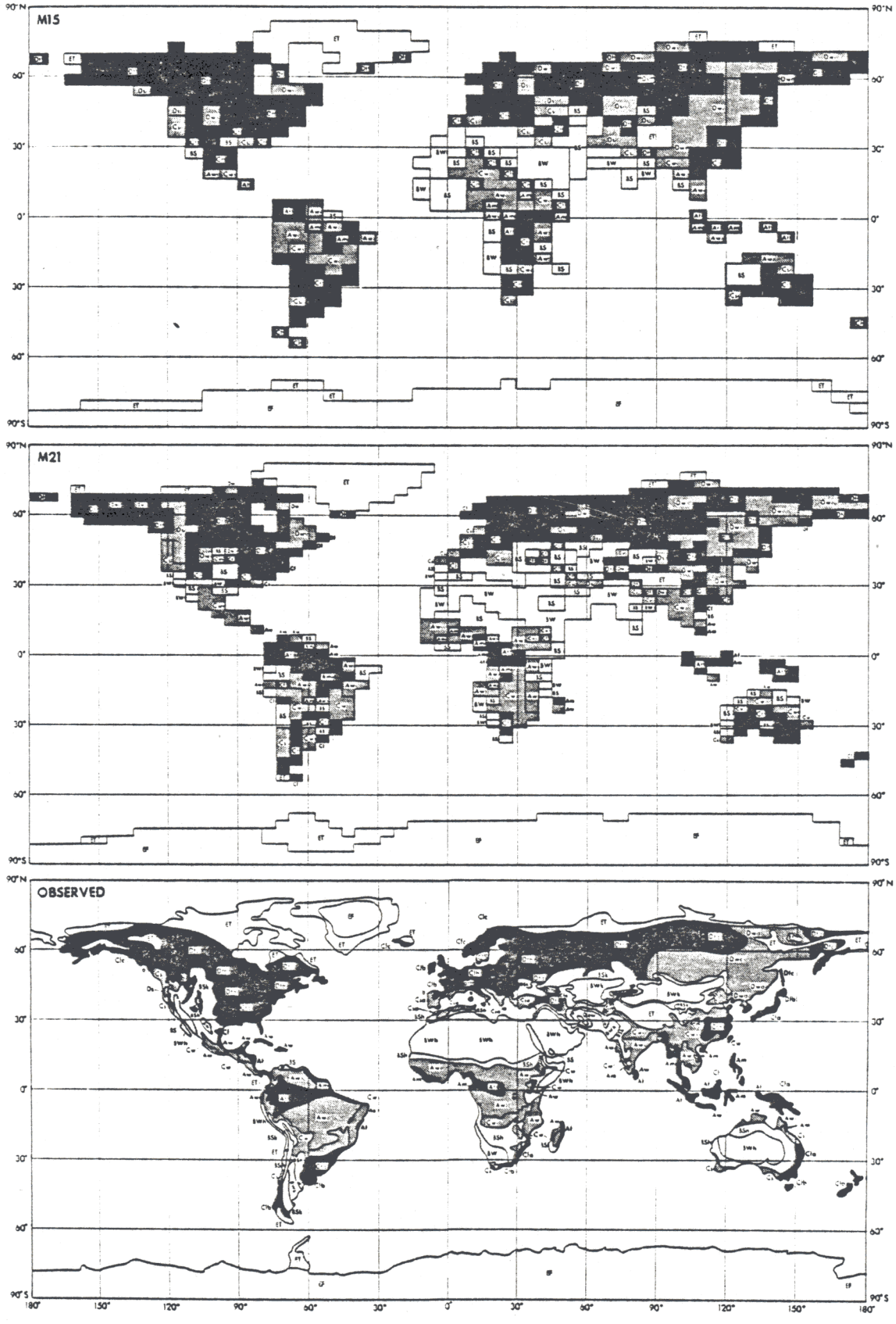

Fig. 14. Global distributions of Köppen climate types as derived from simulated data of the M15 and M21 spectral models and as derived from observed data (Trewartha, 1968).

in the M21 simulation, the Sahara Desert is more realistically expanded, and the tropical rainforest of equatorial North Africa is somewhat better simulated. Common failures of both the M15 and M21 Köppen simulations include an unrealistically narrow Gobi desert and a lack of well-defined desert climates over western North America and southern South America. However, some of these difficulties are expected to be removed or partially removed in a higher resolution spectral simulation of climate because the seasonal variation of precipitation has previously been shown to be much better simulated by the M30 model.

5. Comparison with Grid Models

In this section, an attempt is made to compare the performance of the spectral models with that of grid models which have been developed at the Geophysical Fluid Dynamics Laboratory. Two grid models will be presented for comparison with the spectral models, i.e., a 500 km grid model and a 250 km grid model. Results from simulation experiments using these grid models have been previously published (see Sections 2,3).

The physics of the grid models is nearly identical with that of the spectral models (see Section 2). For the finite differencing, an irregular, energy-conserving global grid system is used (Kurihara and Holloway, 1967). In this system, the north-south separation between grid boxes is constant and the number of grid boxes along each latitude circle decreases poleward thereby giving nearly uniform horizontal grid resolution over the entire globe.

Since the physics of all the models is nearly identical, the ensuing comparisons will hopefully lead to an understanding regarding (1) the dependence of grid model performance on grid resolution and how this compares with the dependence of grid model performance on grid resolution and how this compares with the dependence of spectral model performance on spectral resolution, and (2) the performance of spectral vs. Kurihara-Holloway grid representations of the dynamical equations.

5.1. *Sea level pressure*

January mean sea level pressure profiles of the 500 km and 250 km

grid models are shown in Fig. 15. General failures of both grid models include: polar pressures which are much too high, an equatorward shifting of the large-scale pressure features (i.e., subpolar low pressure belts near 60N and 60S, and subtropical high pressure belts near 30N and 30S) and a very weak pressure gradient from 30S to 60S resulting in very weak westerlies in the Southern Hemisphere. The shortcomings of the simulations listed here are particularly evident in the results from the 500 km grid model. In the spectral model simulations, all of these grid model failures are removed or partly removed, as Fig. 3 indicates. In addition, it is very clear that as the grid resolution is increased, the January profiles of sea level pressure are greatly improved. This is in marked contrast to results obtained from the spectral models where the improvement of the simulation of zonal mean sea level pressure is much more gradual as the resolution is increased.

Geographical distributions of the January and July mean sea level pressure as simulated by the 250 km grid model are presented in Fig. 16 together with the observed counterparts. For additional comparison, a 500 km grid model simulation of sea level pressure is found in Holloway and Manabe (1971). As previously mentioned, the performance of the low resolution (M15) spectral model (as shown in Figs. 2 and 4) is better than expected, and many of its good features are very similar to those obtained by the high resolution (250 km) grid models. For example, in January the subtropical highs west of Africa and South America and the continental lows over Africa and South America seem to be well simulated by both models. Unfortunately, the M15 spectral and 250 km grid models also share some common failures in simulating the horizontal distribution of sea level pressure. In January, examples include a Siberian High which is too intense and an Aleutian low which is too deep.

While there are several examples illustrating that the M15 spectral and the 250 km grid models share in many successes as well as failures, it is perhaps even more significant to note that there are also many examples which illustrate that the low resolution (M15) spectral model outperforms the high resolution (250 km) grid model. In July, the subtropical highs in the North Atlantic and North Pacific are more intense in the spectral model results; the unrealistic low pressure trough over

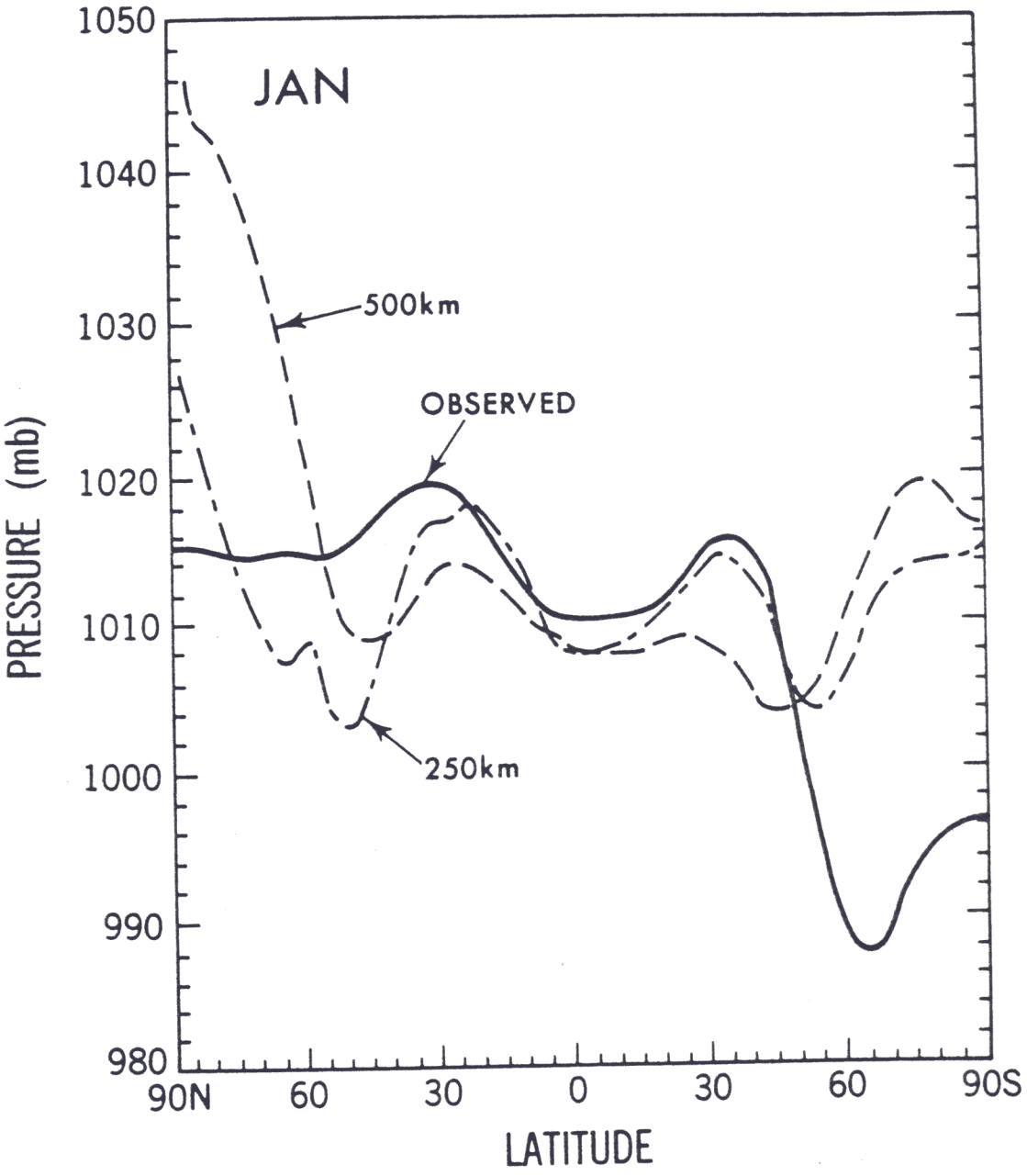

Fig. 15. Latitudinal distributions of the January zonal mean sea level pressure (mb) for the 500 km grid model, the 250 km grid model, and the observed (Crutcher and Meserve, 1970, and Taljaard *et al.*, 1969).

Fig. 16. Geographical distributions of monthly mean sea level pressure (mb) for the 250 km grid model (top) and corresponding observed distributions (Crutcher and Meserve, 1970, and Taljaard *et al.*, 1969) (bottom). Left: mean January distributions; right: mean July distributions.

the western Pacific along the path of many tropical disturbances in the 250 km grid model is absent in the spectral model result; and the position of the South Asian low pressure belt is more realistically shifted westward toward Arabia by the spectral model. For January and July, both models share an inability to simulate the low pressure belt along the Antarctic coast. However, the performance of the low resolution spectral model seems to be better in this regard as the low centers in the 250 km grid model are weaker and are shifted equatorward from their observed positions.

In conclusion, the overall performance of the low resolution spectral model in simulating the large-scale sea level pressure distributions is equal to, or slightly better than, that of the high resolution (250 km) grid model. It goes without saying that the higher resolution spectral models (M21, M30) outperform the 250 km grid model in this regard. One of the important exceptions to this generalization is that the January simulations of the higher resolution spectral models contain a midlatitude belt of exaggerated surface westerlies in the Northern Hemisphere as discussed in Section 4. On the other hand, the higher resolution spectral models accurately simulate the subpolar low pressure belt in the Southern Hemisphere, whereas the grid model simulations fail to reproduce this feature of the Southern Hemisphere sea level pressure distribution accurately.

5.2. *Eddy kinetic energy*

Hemispheric integrals of January mean eddy kinetic energy are contained in Table 5 for both the 500 km and 250 km grid model simulations. These values should be compared with the corresponding spectral model integrals of Table 2. According to Table 5, the eddy kinetic energy simulated by the 500 km grid model is much less than that obtained by the spectral models. This is a result of the use of a large coefficient of nonlinear viscosity which is required to prevent excessive development of computational modes (i.e., checkerboard patterns*) in grid models. In the 500 km grid model as described by Manabe *et al.* (1970a),

*Note that the formulation of the subgrid-scale viscosity for the grid models differs from that of the spectral models.

Table 5. January and July hemispheric integrals of eddy kinetic energy (joules/kg) from the surface to 150 mb of the 500 km and 250 km grid models and corresponding observed integrals (Oort, 1971).

	JANUARY		JULY	
	NH	SH	NH	SH
500 km	60.0	39.0	--	--
250 km	71.8	45.4	41.3	64.1
Obs.	105.4	--	54.4	--

nonlinear viscosity dissipates kinetic energy at not only the grid scale, but also at the scale of synoptic disturbances. Thus, it follows that the kinetic energy of large scale disturbances is maintained at relatively low levels.

Although it is shown in Section 4 that, with low-viscosity, an excessive accumulation of eddy kinetic energy occurs in the highest wave numbers of the M15 spectral model, it does not nullify the validity of its numerical time integration. On the other hand, a significantly smaller nonlinear viscosity coefficient in the 500 km grid model results in an excessive development of checkerboard patterns. In other words, low resolution spectral models, unlike low resolution grid models, do not require as much viscous damping in order to maintain computational stability, and, as a result, are able to maintain more realistic levels of eddy kinetic energy.

According to the formulation of nonlinear viscosity by Smagorinsky (1963), the coefficient of nonlinear viscosity is to be reduced by a factor of four when the grid size is reduced from 500 km to 250 km. Despite the reduction of the coefficient in the 250 km grid model, excessive development of computational modes does not occur because the grid scale is further separated from the scale of baroclinic instability. Owing to the smallness of the coefficient of nonlinear viscosity and the separation of the characteristic scale of dissipation from that of baroclinic instability, the eddy kinetic energy obtained by the 250 km grid model is larger than that of the 500 km grid model simulation as

Table 5 indicates. The latitude-pressure distributions of zonal mean eddy kinetic energy in Fig. 17 indicate that eddy kinetic energy is reduced markedly in the midlatitudes when the grid resolution is reduced from 250 km to 500 km. Although somewhat lower than observed in the actual atmosphere, the level of eddy kinetic energy of the 250 km grid model is comparable with that of the spectral models given in Table 2 and Fig. A2.

Table 6 contains the January mean eddy kinetic energy statistics of the grid model simulations separated into stationary and transient components. These results indicate that both grid models tend to maintain

Table 6. Same as Table 5 for the stationary and transient components of eddy kinetic energy.

	JANUARY		JULY	
STATIONARY	NH	SH	NH	SH
500 km	16.4	7.7	--	--
250 km	32.0	11.4	15.1	15.0
Obs.	16.5	--	7.8	--
TRANSIENT				
500 km	43.6	31.3	--	--
250 km	39.8	35.4	26.2	49.1
Obs.	88.9	--	46.6	--

too much stationary eddy kinetic energy while they are unable to produce enough transient eddy kinetic energy. This inability to partition the eddy kinetic energy accurately between stationary and transient components is also common to all of the spectral simulations (see Table 3 and Table 4).

5.3. *Rate of precipitation*

January and July mean geographical distributions of the rate of

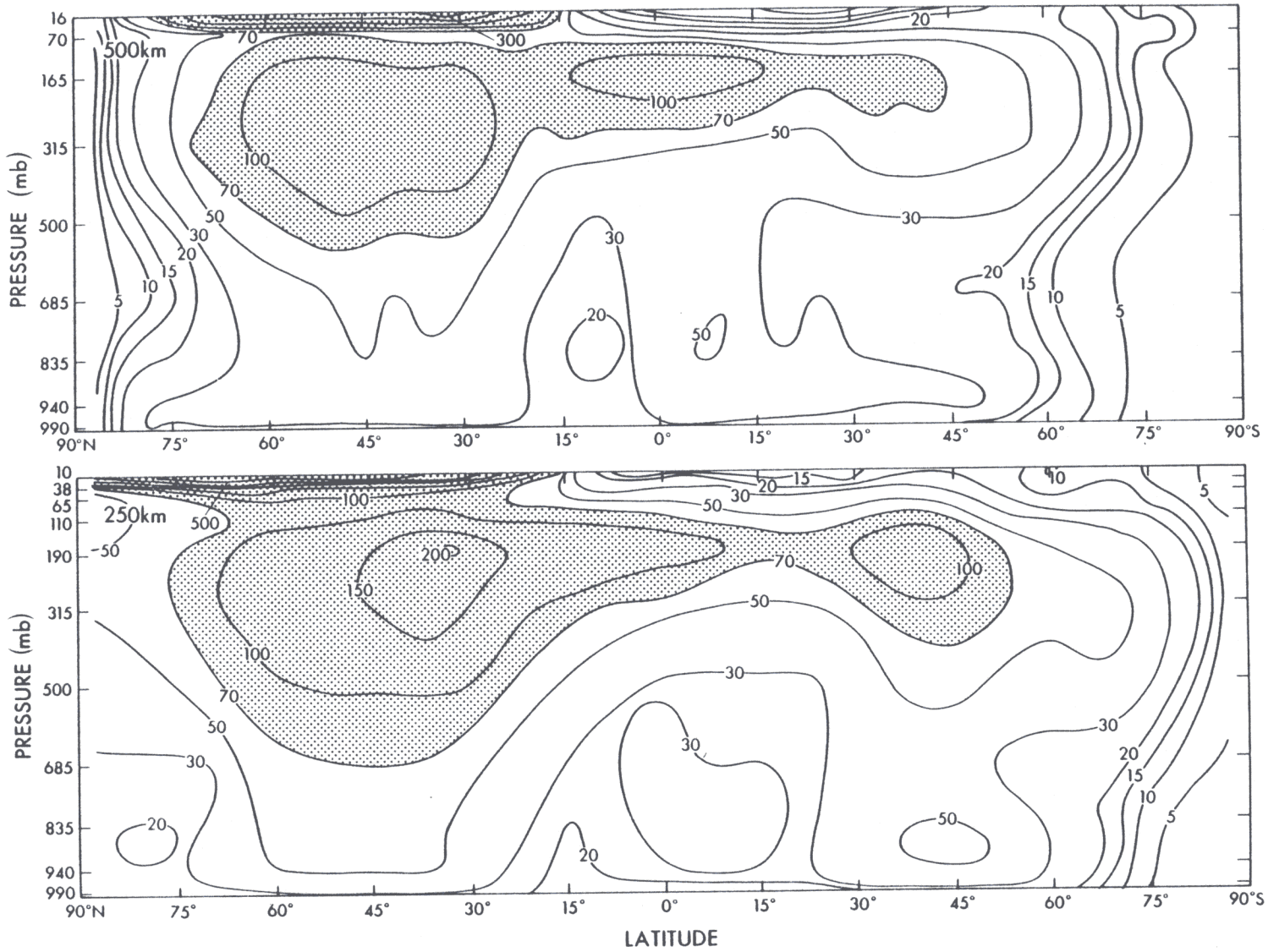

Fig. 17. Cross sections of January zonal mean eddy kinetic energy (J/kg) as simulated by the 500 km grid model (top) and the 250 km grid model (bottom).

precipitation simulated by the 250 km grid model are shown in Fig. 18. Also included in Fig. 18 is the January mean distribution obtained from the 500 km grid model simulation. As previously mentioned, the 500 km grid model has the shortcoming that the large scale sea level pressure features tend to be systematically shifted equatorward (Fig. 15) in its simulation. As a result, similar problems are seen in the rainfall distribution. For example, in January over the eastern North Pacific, the midlatitude rainbelt and the subtropical dry zone tend to be shifted equatorward from their observed positions, and, in the Southern Hemisphere, the midlatitude rainbelt is shifted northward by about 10 degrees from the observed latitude of 50S. In results from the high resolution 250 km grid model the large scale sea level pressure features are more accurately positioned. However, the position of the midlatitude rainbelt of the Southern Hemisphere in the grid model simulation is too far north, even at 250 km resolution. This type of problem is not as pronounced in any of the spectral simulations since the latitudinal positions of the large scale sea level pressure features tend to be more accurately simulated by the spectral models (see Figs. 3 and 5).

Within the tropics and subtropics the 250 km grid model simulation of the rate of precipitation is of very high quality. Even the 500 km grid model simulation of rainfall in the tropics and subtropics has many good qualities. For example, in January the 500 km grid model is able to simulate a rather narrow tropical rainbelt over the eastern Pacific. This good feature of the low resolution grid model simulation is not as pronounced in the low resolution M15 spectral model precipitation patterns (refer to Fig. 11). However, the high resolution M30 spectral model is able to simulate a narrow tropical rainbelt in the eastern Pacific in both months as Figs. 11 and 12 indicate.

In January, the 500 km grid model simulates precipitation rates which are too high over western Asia and central North America. This problem is even more evident in the M15 spectral model. However, in the grid as well as the spectral model simulations, rainfall rates are reduced in these areas by increasing the model resolution. Also in common with spectral model simulations, the tropical rainbelt of the eastern Pacific simulated by grid models tends to be narrowed as the model resolution

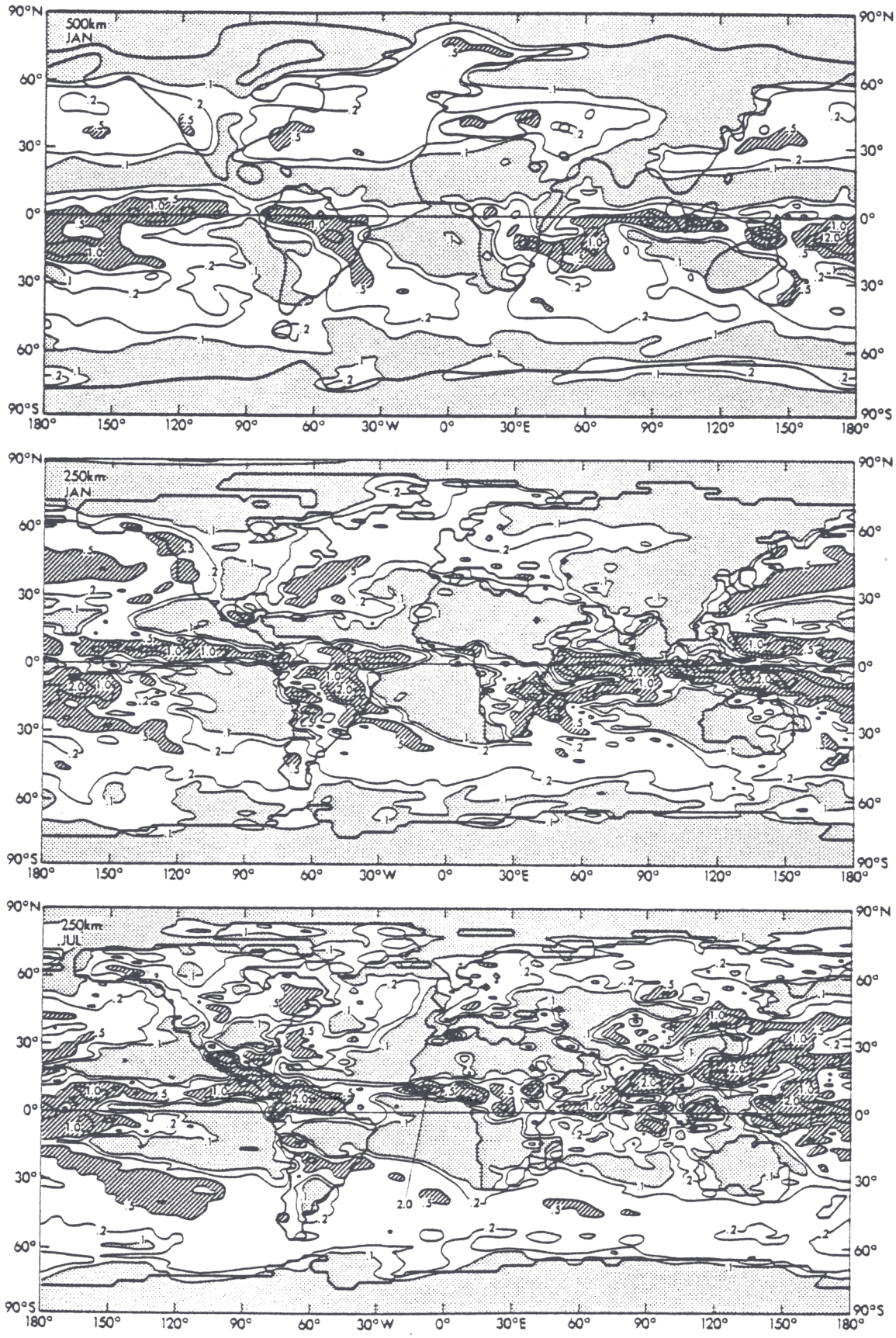

Fig. 18. Geographical distributions of rate of precipitation (cm/day). Top: January mean of the 500 km grid model; middle: January mean of the 250 km grid model; bottom: July mean of the 250 km grid model.

is increased. In general, both grid and spectral coarse resolution models have many difficulties simulating the precipitation distribution; however, the high resolution 250 km grid and the M30 spectral models are relatively free of most of these difficulties and produce precipitation distributions which overall are quite comparable and of very high quality.

6. Computer Requirements

Each of the spectral models was time-integrated using the Advanced Scientific Computer (ASC), designed and constructed by Texas Instruments. Table 7 shows the amount of central processor unit (CPU) time required

Table 7. Time step intervals and amount of computer time required to time-integrate one model day for the M15, M21 and M30 spectral models and for the 500 km and 250 km grid models.

Model		Δt (min)	ASC CPU Time (min/day)
Spectral	M15	30	2
	M21	20	6
	M30	15	18
Latitude-Longitude Grid	d = 500 km	9	7
	d = 250 km	3.75	35

to time-integrate over the period of one model day. Unfortunately, corresponding computer time requirements are not available for the grid models previously discussed since they were not time-integrated on the ASC computer. For comparison purposes, the time requirements of comparable resolution latitude-longitude grid models, described by Manabe *et al.* (1975), are substituted in Table 7. This table indicates that an entire year can be time-integrated by the M15 spectral model in about 12 hours of CPU time.* Similarly, only 36 hours of CPU time are required

*The time requirements for latitude-longitude grid models tend to be underestimates of Kurihara-Holloway grid model computer time requirements since the Kurihara-Holloway grid system is not as intrinsically suitable for array processing on the ASC.

to simulate an entire year by the M21 spectral model which performs at or above the level of the high resolution (250 km) grid model in many respects.

One of the factors accounting for the higher computational speeds of the spectral models is the incorporation of the semi-implicit time integration scheme as previously discussed in Section 2. Note that in Table 7, the time step intervals (Δt) for numerical time integration of the spectral models are much longer than the time intervals for the grid models. The semi-implicit scheme could be incorporated into the grid models, resulting in substantial savings of computer time. Requirements for doing this include solving elliptic equations and a very large amount of computer central memory. However, since grid model incorporation of the semi-implicit time integration scheme is possible, grid model time requirements are not intrinsically as large (relative to those of spectral models) as Table 7 implies.

7. Conclusions

It is shown that the simulated geographical distribution of sea level pressure is dependent on the spectral resolution of the model. For example, the sea level pressure gradients between the subtropics and subpolar latitudes increase with increasing spectral resolution. Accordingly, surface westerlies in middle latitudes of the Southern Hemisphere become stronger and more realistic as the spectral resolution is increased from M15 to M21 and M30. Unfortunately, in January, surface westerlies in middle latitudes of the Northern Hemisphere become stronger and more unrealistic as the spectral resolution is increased. The reason for this difficulty has not yet been identified. With the notable exception of the northern hemisphere winter simulation, the overall performance of a spectral model in simulating the sea level pressure distribution improves with increasing spectral resolution. This generalization is particularly valid for the simulation of sea level pressure in July.

In spite of the high degree of spectral truncation of the M15 model, the M15 simulation of the upper tropospheric flow in lower latitudes is generally successful. A major weakness, however, is the M15 model's inability to simulate detailed flow patterns of the tropics and subtropics,

often resulting in reduced cross-equatorial flow. The high resolution spectral model is able to resolve these difficulties and it, therefore, produces 200 mb flow distributions which appear to be of high quality.

There is no doubt that the geographical distribution of precipitation rate becomes more realistic with increasing spectral resolution. For example, the tropical rainbelt becomes narrower and is defined better and subtropical dry zones become broader as the spectral resolution is increased from M15 to M30. In the M15 spectral model simulation, only the large scale features of the geographical distribution of precipitation rate are simulated. For a more detailed and realistic simulation of climate, the spectral resolution must be increased at least to M21.

All spectral models maintain a level of eddy kinetic energy which is less than that of the actual atmosphere. However, as compared with most general circulation models developed so far, their levels of eddy kinetic energy are relatively high. It is important to note that all spectral models partition too much of their eddy kinetic energy into the stationary component, leaving too little eddy kinetic energy in the transient component.

Although the coefficient of subgrid scale viscosity is initially chosen to be identical in all three spectral models, present results suggest the value of the coefficient of viscosity should be dependent upon the spectral resolution of the model. In the M15 model, eddy kinetic energy tends to accumulate excessively near the wave number of spectral truncation. This result suggests that an increase of the subgrid scale viscosity coefficient would be appropriate. On the other hand, the M30 spectral model tends to underestimate the amplitude of westerly waves, indicating that reducing the coefficient of viscosity would give better results.

Comparisons of results from spectral models with those from Kurihara-Holloway grid models show that spectral models are able to outperform the grid models in simulating the large-scale sea level pressure distribution. In particular, the low resolution M15 spectral model performance is equal to or slightly better than that of the high resolution grid model. While both the 250 km grid and the spectral models share a

tendency to exaggerate the January subpolar low pressure belt near 60N, all three spectral models tend to be superior to the grid models in simulating the subpolar low pressure belt near 60S. For grid models, the simulated sea level pressure distributions deteriorate substantially as the resolution is decreased from a 250 km grid to a 500 km grid. For the spectral models, this deterioration resulting from a reduction in resolution is significantly less.

The spectral models maintain relatively high levels of eddy kinetic energy regardless of spectral resolution, while the eddy kinetic energy of the grid models is reduced as the resolution is decreased from 250 km to 500 km. This reduction partly results from the increase of the subgrid scale viscosity coefficient with increasing grid size as prescribed in the formulation of nonlinear viscosity. In practice, the choice of a relatively large viscosity coefficient is required in a low resolution grid model in order to suppress the excessive growth of computational modes. A common shortcoming of both the grid models and the spectral models is the inability to partition their eddy kinetic energy between stationary and transient components realistically.

The grid model's greatest asset is its ability to simulate the geographical distribution of the rate of precipitation, particularly in tropical and subtropical regions. This is evidenced by the fact that the coarse resolution 500 km grid model is able to simulate some of the large scale precipitation features despite its poor simulation of sea level pressure. On the other hand, the large scale precipitation features are poorly simulated in the low resolution M15 spectral simulation. In order to simulate well-defined tropical oceanic rainbelts and continental dry zones, results which are nearly comparable with those of the high resolution 250 km grid model, one must use spectral resolutions of at least M21. In general, the M30 spectral simulations equal the high level of performance of the 250 km grid model in simulating the hydrologic cycle.

It is important to keep in mind that the performance of the GFDL grid models may not necessarily be similar to the performance of grid models which are constructed by other modeling groups. Refer to other contributions in this report for a detailed description of the performance of other grid models.

In conclusion, it is shown that the spectral models which are described here successfully reproduce many of the large-scale characteristics of climate. Owing to the ease of incorporating the so-called "semi-implicit" time differencing scheme, it is possible to time-integrate a spectral model with relatively little computer time. Therefore, a spectral model is a very convenient tool for carrying out a large number of experiments. In particular, if an experiment does not require a detailed hydrologic simulation, the low resolution M15 spectral model is very useful for obtaining preliminary results with a limited amount of computer time.

Acknowledgments

It is a pleasure to acknowledge C. T. Gordon, who developed a semi-spectral model and kindly made it available as a dynamical framework for our climate model. Clearly, this study could not have existed without his contribution. We are very grateful to W. Stern, who collaborates with C. T. Gordon, for his advice in reprogramming and in adapting their spectral model's dynamics for incorporation into our climate simulation model. W. Bourke of the Australian Numerical Meteorology Research Center, who has been a visiting scientist at GFDL, gave valuable advice throughout the course of this study. Wholehearted support of J. Smagorinsky, Director of GFDL, is sincerely appreciated. We acknowledge L. Dimmick and E. Green, who contributed to the analysis of the results. P. Tunison and his staff, J. Conner, B. Williams and E. Thompson, assisted in the preparation of the figures and the manuscript.

APPENDIX

A. Derivation of the Topography

The topography of the earth's surface used in the M15, M21 and M30 spectral models is shown in Fig. A1. The basic data for the land surface elevations is taken from Scripps Institution of Oceanography data (Smith *et al.*, 1966). The Scripps data are interpolated to a two degree latitude-longitude grid having Gaussian spacing in the north-south

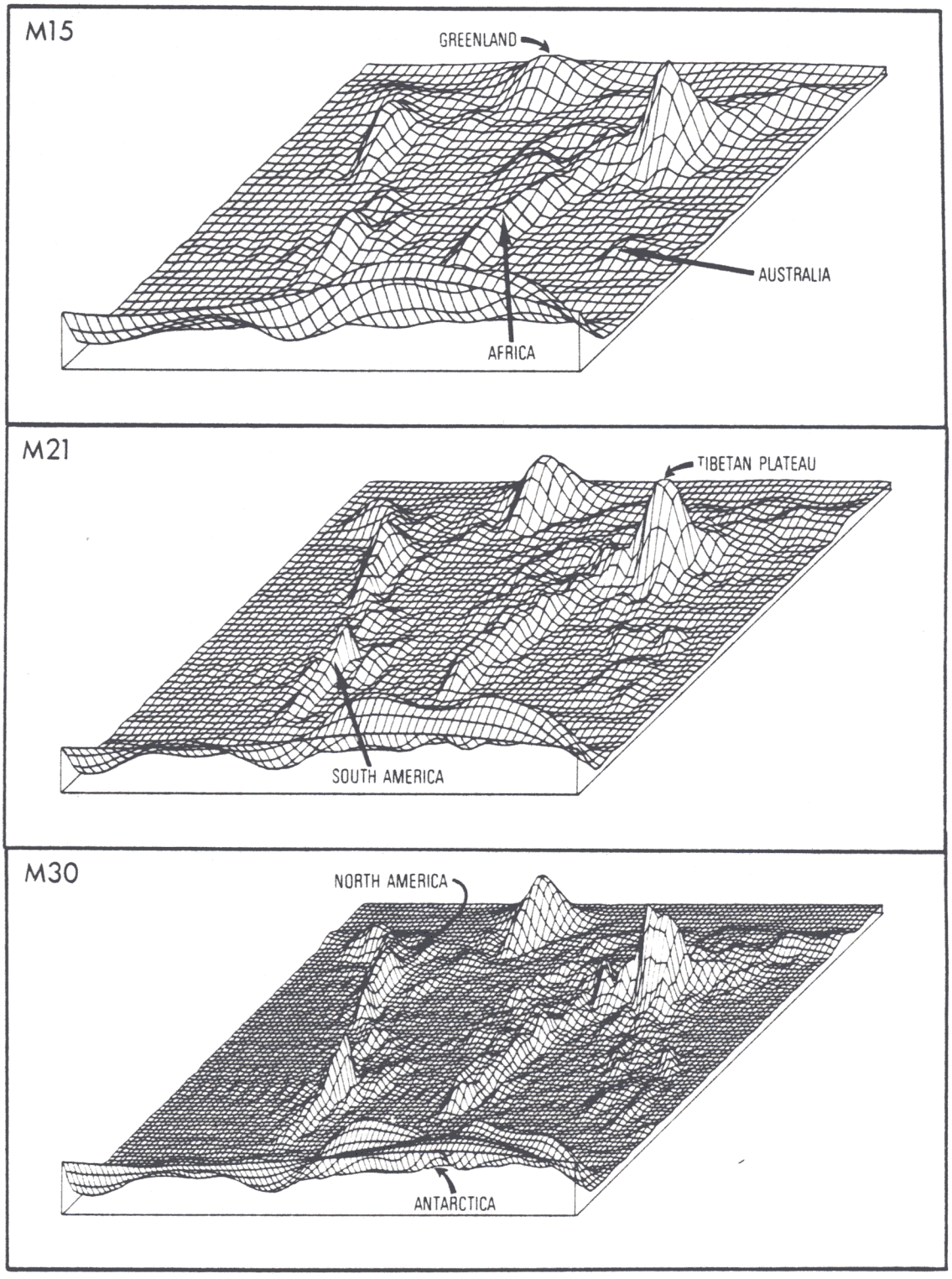

Fig. A1. Three-dimensional distributions of topography (vertical coordinate is exaggerated) for the M15, M21 and M30 spectral models.

direction. These data are smoothed slightly by a simple linear filter in two-dimensions. These grid point topographic heights are then transformed to spectral space having rhomboidal truncation of the appropriate level (M15, M21 or M30). For the M15 spectral model, this method of deriving the topography results in mountains which are less smooth than those derived by Bourke (1977) for his model having the same spectral resolution. However, this method produces more wave-like variations in topography over oceanic areas, e.g., see the Pacific region west of South Africa.

B. Cross Sections of Temperature, Zonal Wind, Meridional Streamfunction and Eddy Kinetic Energy

Meridional cross-sections for the January distributions of temperature, zonal wind, meridional mass transport streamfunction and eddy kinetic energy are shown in Figs. A2 and A3 as given by the M30 spectral model.

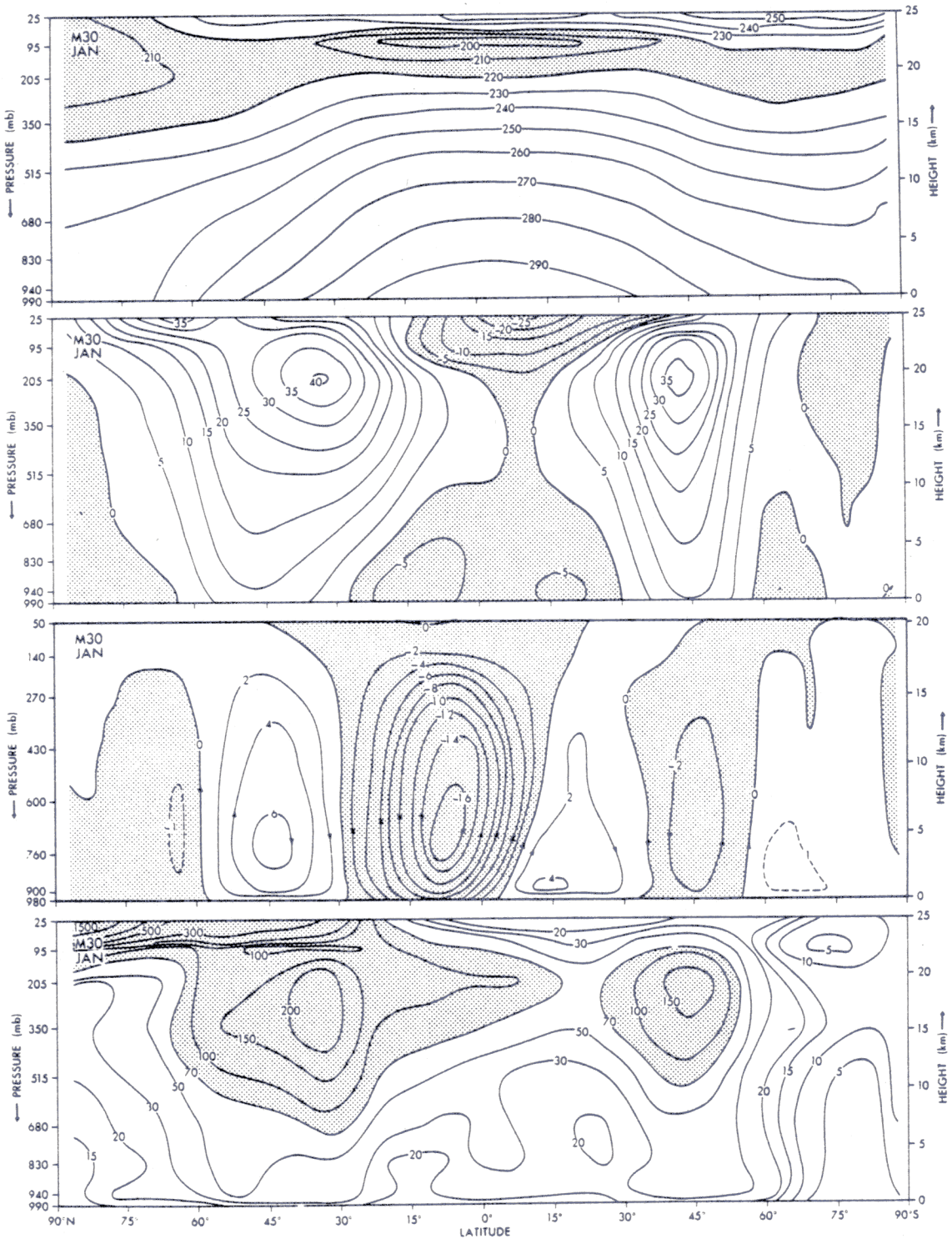

Fig. A2. Cross sections of zonal mean January fields as simulated by the M30 spectral model. Top: temperature (K); second from top: zonal wind (m/s); third from top: meridional streamfunction (10"kg/sec); bottom: eddy kinetic energy (J/kg).

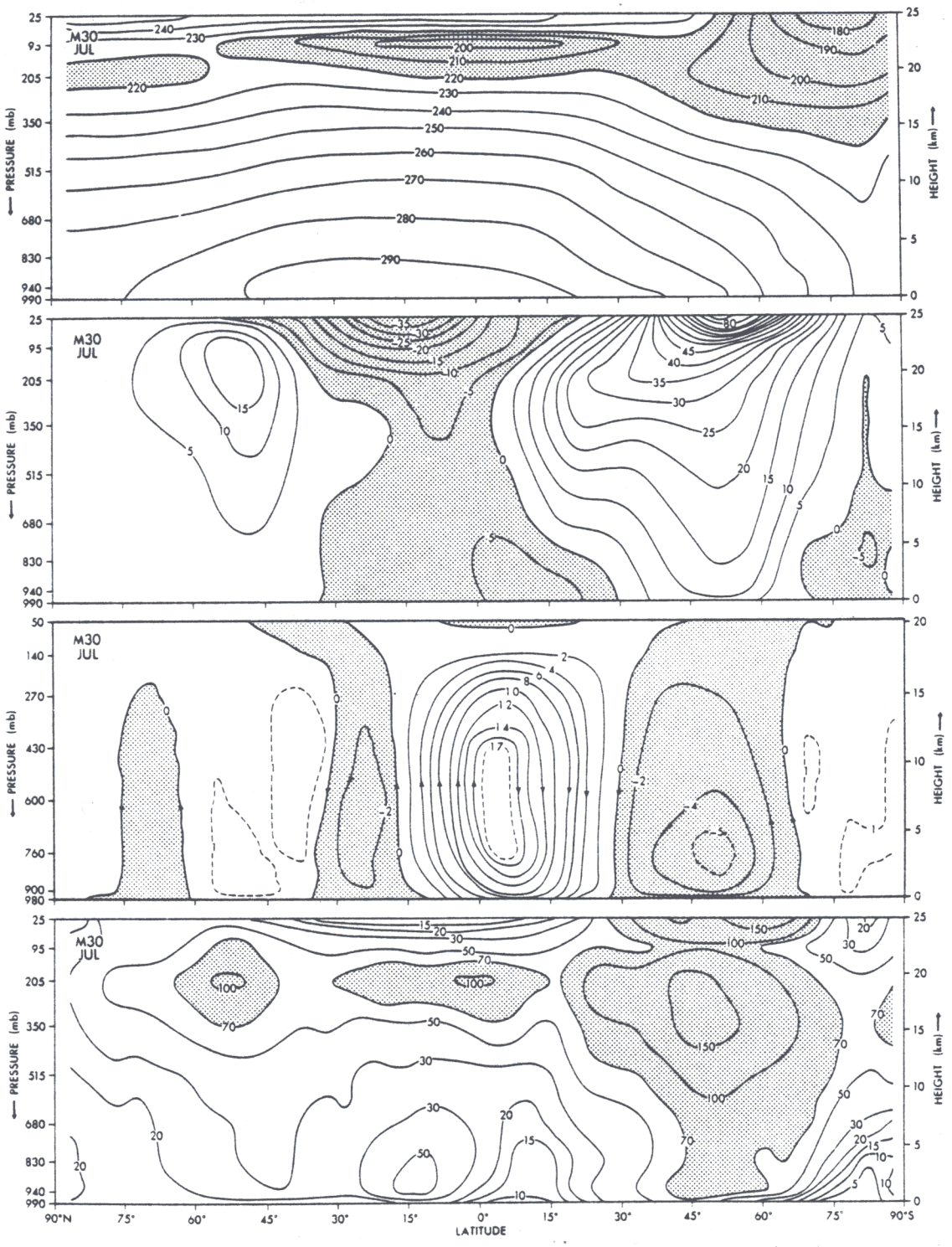

Fig. A3. Cross sections of zonal mean July fields as simulated by the M30 spectral model. Top: temperature (K); second from top: zonal wind (m/s); third from top: meridional streamfunction (10"kg/sec); bottom: eddy kinetic energy (J/kg).

REFERENCES

Bourke, W., 1974. A multi-level model. I. Formulation and hemispheric integrations. *Mon. Wea. Rev., 102,* 688-701.

Bourke, W., B. McAvaney, K. Puri and R. Thurling, 1977. Global modeling of atmospheric flow by spectral methods. *Methods in Comp. Phys., 17,* 267-324.

Crutcher, H. L., and J. M. Meserve, 1970. Selected level heights, temperatures and dew points for the Northern Hemisphere. NAVAIR 50-1C-52, U.S. Naval Weather Serv., Washington, D.C.

Eliasen, E., B. Machenhauer and E. Rasmusson, 1970. On a numerical method for integration of the hydrodynamical equations with a spectral representation of the horizontal fields. Rept. No. 2, Institut for Teoretisk Meteorologi, Köbenhavns Universitet, Denmark.

Haurwitz, B., and J. M. Austin, 1944. *Climatology,* McGraw-Hill, New York.

Holloway, J. L., Jr., and S. Manabe, 1971. Simulation of climate by a global general circulation model. I. Hydrologic cycle and heat balance. *Mon. Wea. Rev., 99,* 335-370.

Hoskins, J. J., and A. J. Simmons, 1975. A multi-layer spectral model and the semi-implicit method. *Quart. J. Roy. Meteor. Soc., 101,* 637-655.

Köppen, W., 1931. *Grundriss der Klimakunde,* Walter de Gruyter, Berlin.

Krishnamurti, T. N., E. G. Astling and M. Kanamitsu, 1975. 200 mb wind field, June, July, August 1972. Dept. Meteor., Florida State University, Tallahassee.

Krishnamurti, T. N., S. M. Daggupaty, J. Fein, M. Kanamitsu and J. D. Lee, 1973. Tibetan high and upper tropospheric tropical circulations during northern summer. *Bull. Amer. Meteor. Soc., 54,* 1234-1249.

Kurihara, Y., and J. L. Holloway, Jr., 1967. Numerical integration of a nine-level global primitive equations model formulated by the box method. *Mon. Wea. Rev., 95,* 509-530.

Manabe, S., J. Smagorinsky and R. F. Strickler, 1965. Simulated climatology of a general circulation model with a hydrologic cycle. *Mon. Wea. Rev., 93,* 769-798.

Manabe, S., 1969. Climate and ocean circulation, Part 1. The atmospheric circulation and hydrology of the earth's surface. *Mon. Wea. Rev., 97,* 739-774.

Manabe, S., J. L. Holloway, Jr. and H. M. Stone, 1970a. Simulated climatology of a general circulation model with a hydrologic cycle, III. Effects of increased horizontal computational resolution. *Mon. Wea. Rev., 98,* 175-212.

Manabe, S., J. L. Holloway, Jr., and H. M. Stone, 1970b. Tropical circulation in a time-integration of a global model of the atmosphere. *J. Atmos. Sci., 27,* 580-613.

Manabe, S., and T. B. Terpstra, 1974. The effects of mountains on the general circulation of the atmosphere as identified by numerical experiments. *J. Atmos. Sci., 31,* 3-42.

Manabe, S., D. G. Hahn and J. L. Holloway, Jr., 1974. The seasonal variation of the tropical circulation as simulated by a global model of the atmosphere. *J. Atmos. Sci., 31,* 43-83.

Manabe, S., and J. L. Holloway, Jr., 1975. The seasonal variation of the hydrologic cycle as simulated by a global model of the atmosphere. *J. Geophys. Res., 80,* 1617-1649.

Manabe, S., K. Bryan and M. J. Spelman, 1975. A global ocean-atmosphere climate model, Part I. The atmospheric circulation. *J. Phys. Ocean, 5,* 3-29.

Möller, F., 1951. Quarterly charts of rainfall for the whole earth (in German). *Petermanns Geograph. Mitt., 95,* 1-7.

Oort, A. H., and E. Rasmusson, 1971. Atmospheric circulation statistics. NOAA Prof. Paper No. 5, U.S. Dept. Commerce, Washington, D.C., 323 pp.

Orszag, S. A., 1970. Transform method for the calculation of vector-coupled sums: Application to the spectral form of the vorticity equation. *Mon. Wea. Rev., 102,* 688-701.

Rao, M.S.V., W. V. Abbot III and J. S. Theon, 1976. Satellite derived global oceanic rainfall atlas (1973 and 1974). National Aeronautics and Space Administration, Washington, D.C., NASA sp-410.

Robert, A. F., 1966. The integration of a low-order spectral form of the primitive meteorological equations. *J. Meteor. Soc. Japan, 44,* 237-245.

Sadler, J. C., 1975. The upper tropospheric circulation of the global tropics. UHMET 75-05, Dept. Meteor., University of Hawaii, Honolulu.

Smagorinsky, J., 1963. General circulation experiments with primitive equations, I. The basic experiment. *Mon. Wea. Rev., 93,* 99-164.

Smith, S. M., H. W. Menard and G. F. Sharman, 1966. World-wide ocean depths and continental elevations averaged for areas approximating one degree squares of latitude and longitude. SIO Ref. Rpt. 65-8, Scripps Institution of Oceanography, La Jolla, 14 pp.

Stone, H. M., and S. Manabe, 1968. Comparison among various numerical models designed for computing infrared cooling. *Mon. Wea. Rev.*, *96*, 735-751.

Taljaard, J. J., H. van Loon, H. L. Crutcher and R. L. Jenne, 1969. Climate of the upper air, 1. Southern Hemisphere. Vol. 1. Temperatures, dew points, and heights at selected pressure levels. NAVAIR 50-1C-55, U.S. Naval Weather Serv., Washington, D.C.

Trewartha, G. T., 1968. *An Introduction to Climate*, 4th ed., McGraw-Hill, New York.

U.S. Naval Oceanographic Office (U.S. Navy Hydrographic Office), 1944. World Atlas of Sea Surface Temperatures, 2nd ed., H.O. Publ. No. 225, Washington, D.C.

U.S. Naval Oceanographic Office, 1957. Oceanographic Atlas of the Polar Seas, Part I. Antarctic. H.O. Publ. No. 705, Washington, D.C.

U.S. Naval Oceanographic Office, 1958. Oceanographic Atlas of the Polar Seas, Part II. Arctic. H.O. Publ. No. 705, Washington, D.C.

U.S. Naval Oceanographic Office, 1967a. Monthly charts of mean, minimum, and maximum sea surface temperature of the Indian Ocean. SP-99, Washington, D.C.

U.S. Naval Oceanographic Office, 1967b. Oceanographic Atlas of the North Atlantic Ocean, Section II: Physical Properties. Publ. No. 700, Washington, D.C.

U.S. Naval Oceanographic Office, 1969. Monthly charts of mean, minimum, and maximum sea surface temperature of the North Pacific Ocean. SP-123, Washington, D.C.